INTERNATIONAL JOURNAL FOR NUMERICAL METHODS IN FLUIDS
Int. J. Numer. Meth. Fluids 2003; **43**:597–635 (DOI: 10.1002/fld.496)

Effects of blood models on flows through a stenosis

Panagiotis Neofytou[1,*,†] and Dimitris Drikakis[2]

[1] *Department of Mechanical Engineering, University of Manchester Institute of Science and Technology, M60 1QD, Manchester, U.K.*
[2] *Department of Engineering, Queen Mary, University of London, London E1 4NS, U.K.*

SUMMARY

The paper presents a numerical investigation of non-Newtonian modelling effects on unsteady periodic flows in a two-dimensional (2D) channel with a stenosis. The geometry and boundary conditions were chosen so as to reproduce the flow features that are observed in real haemodynamic conditions. Three different non-Newtonian constitutive equations for modelling the shear characteristics of the blood namely the Casson, power-law and Quemada models, are utilized. Similarly with previous studies based on Newtonian modelling, the present simulations show the formation of several vortices downstream of the stenosis, as well as substantial variations of the wall shear stress throughout the unsteady cycle. Additionally, it is shown that: (i) there are substantial differences between the results obtained by Newtonian and non-Newtonian models, and (ii) the prediction of vortex formation, wall shear stress distribution and separation behind the stenosis is strongly dependent on the details of the non-Newtonian model employed in the simulations. Copyright © 2003 John Wiley & Sons, Ltd.

KEY WORDS: haemodynamics; pulsatile flow; non-Newtonian modelling; simulation

1. INTRODUCTION

The role of fluid mechanics in atherogenesis has been investigated for many years in order to determine the flow characteristics that are linked with atherosclerosis formation. So far, it is known that atherosclerotic lesions do not occur randomly in the arterial network, but tend to be localized at sites where blood flow effects differ from those in straight arteries. There is evidence [1] that the localized adhesion of fatty streaks reflects a non-uniformity of the artery-wall permeability. Nerem *et al.* [2] have shown that regions of greatest permeability are well correlated with the regions in which fatty streaks develop in cholesterol-fed animals. Furthermore, they showed that there is direct dependence of the wall permeability on steady shears and reported stronger dependence on the amplitude of oscillatory shear stresses.

* Correspondence to (Present address): P. Neofytou, Environmental Research Laboratory, Institute of Nuclear Technology and Radiation Protection, National Center for Scientific Research 'Demokritos', Agia Paraskevi, 15310 Athens, Greece.
† E-mail: panosn@avra.ipta.demokritos.gr

Received 3 March 2002
Revised 1 December 2002

Experiments by Fry [3] show that maintaining the wall shear stress (WSS) at high levels for a short time causes irreversible damage to the endothelial surface leading, subsequently, to a great enhancing of its permeability. Despite the above studies, the causes of the initiation and progression of the arterial lesions still remain unclear.

Due to the importance of the atherosclerotic disease the understanding of the mechanism of atheromatosis formation has also been attempted through computational fluid dynamics. Several researchers have modelled numerically stenotic arterial flows [4–7]. In these studies a two-dimensional channel was employed, with the flow being considered as unsteady and Newtonian. The investigations aimed at understanding the mechanism of vortex formation [4–9], or the mass transfer rate and WSS distribution [10] behind the stenosis. In a recent study [8], three-dimensional flow effects in stenotic (Newtonian) flows were investigated, including study of instabilities and transition to turbulence. It was found that three-dimensional instabilities share similarities with the instabilities observed in two-dimensional suddenly expanded flows [11]. Physiological flow effects in a 3D non-symmetric geometry of a stenosis have also been numerically studied [12] and showed that the side of the wall with the stenosis experiences a higher shearing stress compared to the other side without any protuberance.

In addition to the Newtonian flow studies, there have been a few investigations based on non-Newtonian modelling of the blood. Buchanan *et al.* [13] employed the Quemada and power-law models for an axisymmetric stenotic channel and investigated the accumulation of flow particles in the vortex formation under a sinusoidal input pulse. Tu *et al.* [9] also used the Herschel–Bulkley model for studying an axisymmetric stenotic flow under unsteady inflow conditions. Srivastava and Saxena [14] studied the flow through stenotic small arteries with the blood represented by a two-fluid Newtonian–Casson model in order to investigate the relation between the WSS and the viscosity of the peripheral layer. Furthermore in the broader field of haemodynamic flows, numerical studies using spectral/*hp* element methods [15] have been carried out in order to encompass more complicated 3D geometries that stem from medical images.

The aim of the present study is to investigate non-Newtonian modelling effects on the unsteady periodic flow through a stenosis using the most well-documented blood constitutive equations, namely the Casson [16], power law [17] and Quemada [18] models. Newtonian and non-Newtonian flow computations have been carried out in order to examine the modelling effects with respect to the vortex formation and WSS distribution. Additionally, a numerical investigation of the flow behaviour at different Strouhal numbers has been conducted. The Strouhal numbers employed here apply to different heart rates corresponding to normal and tachycardial conditions. The computations reveal that the results for the vortex formation and the WSS distribution (especially its peak values) are dependent on the non-Newtonian model employed.

2. MODEL EQUATIONS

2.1. Governing equations

The problem is governed by the Navier–Stokes equations for a two-dimensional incompressible flow. These are the continuity equation

$$\int_S \mathbf{V} \cdot \mathrm{d}\mathbf{S} = 0 \tag{1}$$

where $\mathbf{V}=[u,v]^{\mathrm{T}}$, with u and v being the velocity components in the x and y directions, respectively, and momentum equations

$$\frac{\partial}{\partial t}\int_{\Omega}\rho u\,\mathrm{d}\Omega+\int_{S}\rho u\mathbf{V}\cdot\mathrm{d}\mathbf{S}=-\int_{S}p\mathbf{i}_x\cdot\mathrm{d}\mathbf{S}+\int_{S}(\tau_{xx}\mathbf{i}_x+\tau_{xy}\mathbf{i}_y)\cdot\mathrm{d}\mathbf{S} \tag{2a}$$

$$\frac{\partial}{\partial t}\int_{\Omega}\rho v\,\mathrm{d}\Omega+\int_{S}\rho v\mathbf{V}\cdot\mathrm{d}\mathbf{S}=-\int_{S}p\mathbf{i}_y\cdot\mathrm{d}\mathbf{S}+\int_{S}(\tau_{yx}\mathbf{i}_x+\tau_{yy}\mathbf{i}_y)\cdot\mathrm{d}\mathbf{S} \tag{2b}$$

for the x and y directions respectively. Ω represents volume; $\mathrm{d}\mathbf{S}$ equals to $\mathbf{n}\cdot\mathrm{d}\mathbf{S}$ where $\mathbf{n}$ is the unit vector normal to the surface $\mathrm{d}\mathbf{S}$; $\mathbf{i}_x$, $\mathbf{i}_y$ are the unit vectors in the x and y directions, respectively; p is the pressure and ρ is the density. The equations are solved on a curvilinear body-fitted grid (see also Section 4.1). The shear stress τ in the diffusion terms of (2a) and (2b) are written in terms of the shear rate γ as

$$\tau_{ij}=\mu\gamma_{ij} \tag{3}$$

where $i,j=x,y$. The molecular viscosity coefficient μ is constant for Newtonian flows, whereas it is a function of the shear rate γ in the case of non-Newtonian flows. The shear rate can be written in tensor form as

$$\bar{\boldsymbol{\gamma}}=2\bar{\mathbf{D}}=\nabla\mathbf{V}+\nabla\mathbf{V}^{\mathrm{T}} \tag{4}$$

where $\bar{\mathbf{D}}$ is the deformation tensor. Hence (3) can also be written as

$$\bar{\boldsymbol{\tau}}=\mu\bar{\boldsymbol{\gamma}} \tag{5}$$

where $\bar{\boldsymbol{\tau}}$ is the shear-stress tensor.

Following the *principle of material objectivity*, i.e. μ should remain unchanged regardless of the frame of reference, the expression for $\bar{\boldsymbol{\gamma}}$ involves the second invariant of the rate of deformation tensor II_D, that is

$$|\bar{\boldsymbol{\gamma}}|=\sqrt{2\,\mathrm{tr}(\bar{\mathbf{D}}^2)} \tag{6}$$

Therefore, in the case of non-Newtonian fluids the general relation between μ and $\bar{\boldsymbol{\gamma}}$ is

$$\bar{\boldsymbol{\tau}}=\mu(|\bar{\boldsymbol{\gamma}}|)\bar{\boldsymbol{\gamma}} \tag{7}$$

For two- or three-dimensional numerical simulations, any constitutive equation in simple shear form for viscous non-Newtonian flows should first be written as

$$\boldsymbol{\tau}=\mu(\gamma)\cdot\gamma \tag{8}$$

and then expressed in tensorial form, as in (7), so that $\mu(|\bar{\boldsymbol{\gamma}}|)$, which is referred to as the 'effective viscosity', can be specified. The effective viscosity is then used for the calculation of the diffusion terms in the Navier–Stokes equations.

Substituting (5) into (1) and (2), and non-dimensionalizing all the variables in the governing equations, the diffusion terms (DT) then become

$$\mathrm{DT}'_x = \frac{1}{\rho U_\infty l} \int_{S^*} \mu(\gamma^*_{xx}\mathbf{i}_x + \gamma^*_{xy}\mathbf{i}_y) \cdot \mathrm{d}\mathbf{S}^* \tag{9}$$

$$\mathrm{DT}'_y = \frac{1}{\rho U_\infty l} \int_{S^*} \mu(\gamma^*_{yx}\mathbf{i}_x + \gamma^*_{yy}\mathbf{i}_y) \cdot \mathrm{d}\mathbf{S}^* \tag{10}$$

where the asterisk superscript denotes dimensionless quantities and ρ, U_∞ and l are the reference density, velocity and length, respectively, utilized in the non-dimensionalization. The effective viscosity should be expressed in terms of the non-dimensional $|\bar{\boldsymbol{\gamma}}|$, that is, $\mu(|\bar{\boldsymbol{\gamma}}|^*)$. According to the non-dimensionalization procedure

$$|\bar{\boldsymbol{\gamma}}|^* = \frac{|\bar{\boldsymbol{\gamma}}|}{U_\infty / l} \tag{11}$$

Generally $\mu(|\bar{\boldsymbol{\gamma}}|^*)$ can be decomposed as a product of constant part, say C_0, and a function of $|\bar{\boldsymbol{\gamma}}|^*$, say $f(|\bar{\boldsymbol{\gamma}}|^*)$, so that

$$\mu(|\bar{\boldsymbol{\gamma}}|^*) = C_0 f(|\bar{\boldsymbol{\gamma}}|^*) \tag{12}$$

Inserting (12) into (9) and (10), one can see that a term similar to a Reynolds number results in front of the diffusion terms; this term is defined by

$$Re' = \frac{\rho U_\infty l}{C_0} \tag{13}$$

In the case where μ is constant (that is, Newtonian flow), $C_0 = \mu$ and $f(|\bar{\boldsymbol{\gamma}}|^*) = 1$.

2.2. Non-Newtonian models

Three non-Newtonian constitutive relationships have been employed for modelling the diffusive terms

(i) *Casson model* [16]: This is the most broadly used model to represent the rheological behaviour of blood. Casson's [16] constitutive equation is given by

$$\begin{aligned} \sqrt{\tau} &= \sqrt{\tau_\mathrm{y}} + \sqrt{\mu_\infty \gamma}, \quad && |\tau| > \tau_\mathrm{y} \\ \gamma &= 0, && |\tau| < \tau_\mathrm{y} \end{aligned} \tag{14}$$

where τ_y is the yield stress and μ_∞ is the asymptotic viscosity. According to Charm *et al.* [1, 19] for blood $\tau_\mathrm{y} = 10.82$ mPa and $\mu_\infty = 3.1 \times 10^{-3}$ Pa s. Equation (14) can also be written in the form of (8) as

$$\begin{aligned} \tau &= \left(\sqrt{\frac{\tau_\mathrm{y}}{\gamma}} + \sqrt{\mu_\infty} \right)^2 \gamma, \quad && |\tau| > \tau_\mathrm{y} \\ \gamma &= 0, && |\tau| < \tau_\mathrm{y} \end{aligned} \tag{15}$$

Therefore, its tensorial form is

$$\begin{aligned} \bar{\tau} &= \left(\sqrt{\frac{\tau_y}{|\bar{\gamma}|}} + \sqrt{\mu_\infty}\right)^2 \bar{\gamma}, \quad |\bar{\tau}| > \tau_y \\ \bar{\gamma} &= \mathbf{0}, \qquad\qquad\qquad\quad |\bar{\tau}| < \tau_y \end{aligned} \tag{16}$$

The difficulty in applying Casson's equation in numerical schemes lies in its discontinuous character. Papanastasiou [20] proposed an alternative expression that overcomes this obstacle, that is, one equation for the whole range of shear-stress values. According to Papanastasiou [20], (16) is rewritten as

$$\bar{\tau} = \left[\sqrt{\mu_\infty} + \sqrt{\frac{\tau_y}{|\bar{\gamma}|}}(1 - e^{-\sqrt{m|\bar{\gamma}|}})\right]^2 \bar{\gamma} \tag{17}$$

This equation has been found [21] to approach Casson's equation very satisfactorily for $m > 100$. Comparing (17) with (7), one concludes that the effective viscosity is

$$\mu(|\bar{\gamma}|) = \left[\sqrt{\mu_\infty} + \sqrt{\frac{\tau_y}{|\bar{\gamma}|}}(1 - e^{-\sqrt{m|\bar{\gamma}|}})\right]^2 \tag{18}$$

The dimensionless expression of (18) according to (11) is

$$\mu(|\bar{\gamma}|^*) = \mu_\infty \left[1 + \sqrt{\frac{Bi}{|\bar{\gamma}|^*}}(1 - e^{-\sqrt{m'|\bar{\gamma}|^*}})\right]^2 \tag{19}$$

where $m' = m/l/U_\infty$ and Bi is the Bingham number defined by

$$Bi = \frac{\tau_y l}{\mu_\infty U_\infty} \tag{20}$$

According to (12), in the case of a Casson-model-based flow

$$C_0 = \mu_\infty, \quad f(|\bar{\gamma}|^*) = \left[1 + \sqrt{\frac{Bi}{|\bar{\gamma}|^*}}(1 - e^{-\sqrt{m'|\bar{\gamma}|^*}})\right]^2 \tag{21}$$

and taking into account (13), Re', which in this case is referred to as Re_{CA}, is defined as

$$Re_{CA} = \frac{\rho U_\infty l}{\mu_\infty} \tag{22}$$

The characteristic parameters for a Casson-model-based flow are Re_{CA} and Bi.

(ii) *Power-law model*: We have employed the version of the power-law model as proposed by Walburn and Schneck [17] (this is also referred to as 'Best three variable model'). The model takes into account the haematocrit (H) and the total protein minus albumin (TPMA). The shear stress is given by

$$\tau = k\gamma^n \tag{23}$$

According to Walburn and Schneck [17], for normal blood samples the parameters in (23) are $k = 14.67 \times 10^{-3}$ Pa s^n and $n = 0.7755$. Bringing (23) into the form of (8), we obtain

$$\tau = k\gamma^{n-1}\gamma \tag{24}$$

and its tensorial form is

$$\bar{\tau} = k|\bar{\gamma}|^{n-1}\bar{\gamma} \tag{25}$$

Comparing (25) with (7), one concludes that the effective viscosity is

$$\mu(|\bar{\gamma}|) = k|\bar{\gamma}|^{n-1} \tag{26}$$

Using (11), the dimensionless form of (26) is

$$\mu(|\bar{\gamma}|^*) = k\frac{U_\infty^{n-1}}{l^{n-1}}|\bar{\gamma}|^{*^{n-1}} \tag{27}$$

According to (12), in the case of a power-law-model-based flow

$$C_0 = k\frac{U_\infty^{n-1}}{l^{n-1}}, \quad f(|\bar{\gamma}|^*) = |\bar{\gamma}|^{*^{n-1}} \tag{28}$$

Following (13), Re', which in this case is referred to as Re_{PL}, is given by

$$Re_{\mathrm{PL}} = \frac{\rho l^n}{kU_\infty^{n-2}} \tag{29}$$

The characteristic parameter for a power-law-model-based flow is Re_{PL}.

(iii) *Quemada's model* [18]: Quemada [18] proposed a model, derived to predict the viscosity of concentrated disperse systems, based on shear rate and haematocrit. The shear stress is given by

$$\tau = \mu_F\left(1 - \frac{1}{2}\frac{k_0 + k_\infty\sqrt{\gamma/\gamma_c}}{1+\sqrt{\gamma/\gamma_c}}\varphi\right)^{-2}\gamma \tag{30}$$

where $\mu_{\mathrm{F}} = 1.2 \times 10^{-3}$ Pa s is the viscosity of plasma (suspending medium) and for haematocrit $\varphi = 0.45$ the values of the parameters are $\gamma_c = 1.88\,\mathrm{s}^{-1}$, $k_\infty = 2.07$ and $k_0 = 4.33$. Equation (30) is already written in the form of (8). Its tensorial form would be

$$\bar{\tau} = \mu_F\left(1 - \frac{1}{2}\frac{k_0 + k_\infty\sqrt{|\bar{\gamma}|/\gamma_c}}{1+\sqrt{|\bar{\gamma}|/\gamma_c}}\varphi\right)^{-2}\bar{\gamma} \tag{31}$$

Comparing (31) with (7), one concludes that the effective viscosity is

$$\mu(|\bar{\gamma}|) = \mu_F\left(1 - \frac{1}{2}\frac{k_0 + k_\infty\sqrt{|\bar{\gamma}|/\gamma_c}}{1+\sqrt{|\bar{\gamma}|/\gamma_c}}\varphi\right)^{-2} \tag{32}$$

The dimensionless expression of (32) according to (11) is

$$\mu(|\bar{\gamma}|^*) = \mu_F\left(1 - \frac{1}{2}\frac{k_0 + k_\infty\sqrt{|\bar{\gamma}|^*/\gamma_c^*}}{1+\sqrt{|\bar{\gamma}|^*/\gamma_c^*}}\varphi\right)^{-2} \tag{33}$$

where

$$\gamma_c^* = \frac{\gamma_c}{U_\infty / l} \tag{34}$$

According to (12), in the case of a Quemada-model-based flow

$$C_0 = \mu_F, \quad f(|\bar{\dot{\gamma}}|^*) = \left(1 - \frac{1}{2}\,\frac{k_0 + k_\infty \sqrt{|\bar{\dot{\gamma}}|^*/\gamma_c^*}}{1 + \sqrt{|\bar{\dot{\gamma}}|^*/\gamma_c^*}}\,\varphi\right)^{-2} \tag{35}$$

Taking into account (13), Re', which in this case is referred to as Re_{QU}, is given by

$$Re_{\mathrm{QU}} = \frac{\rho U_\infty l}{\mu_F} \tag{36}$$

The characteristic parameters for a Quemada-model-based flow are Re_{QU} and γ_c^*.

2.3. Geometry and parameters

The geometry of the problem consists of a channel with an arc-shaped stenosis (Figure 1(i)) and is similar to the one used by Rosenfeld [4, 5] for studying the vortex-formation mechanism behind the stenosis. The dimensionless parameters of the channel geometry are $L_{\mathrm{u}} = 7$, $L_{\mathrm{d}} = 28.34$, $H = 1$. The value of the downstream length L_{d} was chosen so that the fully developed velocity profile can be restored at the outlet as it will be later discussed.

The non-dimensionalization and calculation of the dimensionless parameters were based on a mean inlet velocity, U_s (defined later), and the channel height, H. Therefore, the Reynolds (for Newtonian flow) and Strouhal numbers are defined as

$$Re = \frac{\rho U_s H}{\mu}, \quad Str = \frac{H}{U_s T} \tag{37}$$

where T is a characteristic time length in the definition of the problem. The non-Newtonian parameters Re_{PL} and Bi for the Casson, Re_{PL} for the power law, and γ_c^* and Re_{QU} for the Quemada models (Equation (20), (22), (29), (34) and (36), respectively) are written:

$$Re_{\mathrm{CA}} = \frac{\rho U_s H}{\mu_\infty}, \quad Bi = \frac{\tau_{\mathrm{y}} H}{\mu_\infty U_s}, \quad Re_{\mathrm{PL}} = \frac{\rho H^n}{k U_s^{n-2}}, \quad \gamma_c^* = \frac{\gamma_c}{U_s / H}, \quad Re_{\mathrm{QU}} = \frac{\rho U_s H}{\mu_F} \tag{38}$$

The comparison between different Newtonian and non-Newtonian models at a given Reynolds number is based on the same values of U_s and H. For example, if the value of H is known, U_s can be calculated from (37) so that finally all the non-Newtonian parameters in (38) can be calculated. In other words, the comparisons are carried out for the same inflow rate.

2.4. Boundary conditions

The computational boundaries are defined (in dimensionless units) as follows: the wall boundary is at $y = 0$ and $y = 1$ $\forall x \in [0,\ 7] \cup [11.66,\ 40]$ and at $y = 0$ and $y = 1 - (a - R + \sqrt{R^2 - [b/2 - (x - L_{\mathrm{u}})]^2})$ where $R = [a^2 + (b/2)^2]/2a$ $\forall x \in (7, 11.66)$ and $a = 0.56$, $b = 4.66$ (Figure 1(i)). The inflow boundary is at $x = 0$ $\forall y \in [0,\ 1]$ and the outflow boundary is at $x = 40$ $\forall y \in [0, 1]$. At the wall boundary, the pressure values are derived by extrapolation from inside the domain, whereas the velocity boundary value is set equal to zero following

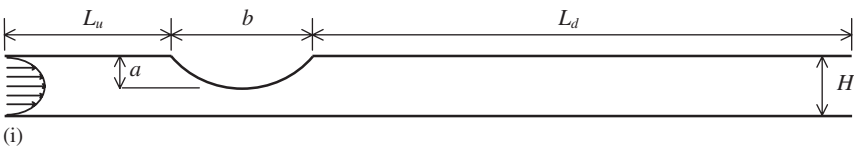

(i)

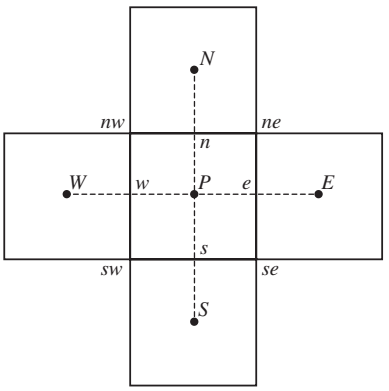

(ii)

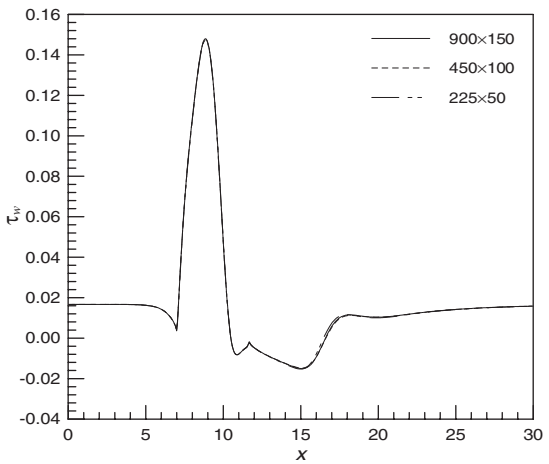

(iii)

Figure 1. (i) Geometry of the channel with a stenosis. (ii) Topology of grid with collocated arrangement of variables. (iii) Grid independence using the upper wall DWSS distribution for the case of a steady Newtonian flow with $Re = 360$. (iv) Comparison of outlet velocity profile between numerical prediction and theory for the Newtonian flow case with $Re = 360$, $Str = 0.05$ at $t/T = 0.7$. (v) Comparison of the upper wall DWSS distribution for the Newtonian flow case with $Re = 360$, $Str = 0.368$ at $t/T = 0.2$ of subsequent cycles of the period. (vi) Comparison of the present results with experimental and numerical data from Rosenfeld [18] and Park [26] for the location of the $B1$ vortex throughout the period (Newtonian case at $Re = 360$ and 180, and $Str = 0.368$). (vii) Streamlines for the steady flow using the Newtonian and non-Newtonian models. (viii) Dimensionless pressure distribution for the steady flow using the Newtonian and non-Newtonian models.

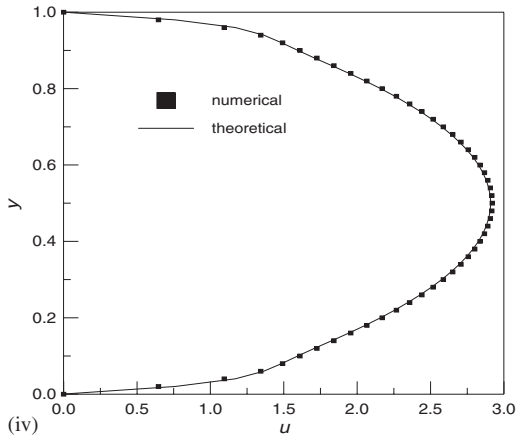

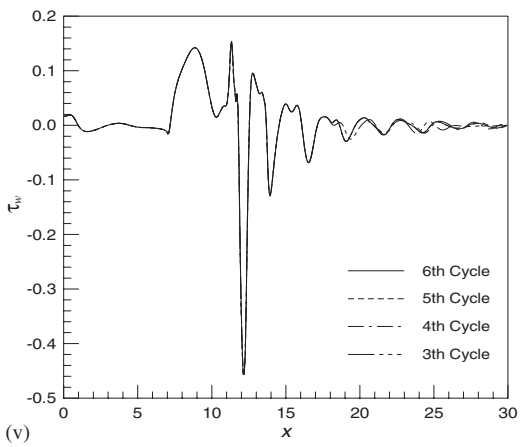

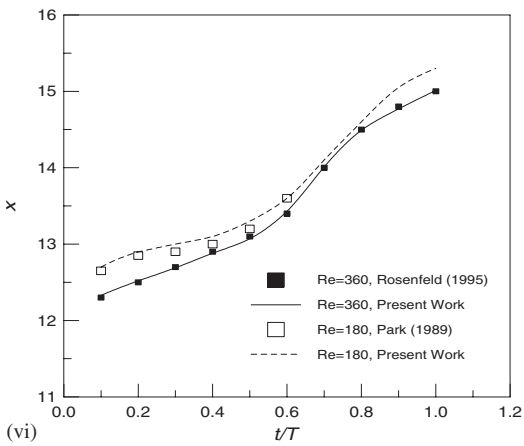

Figure 1. *Continued.*

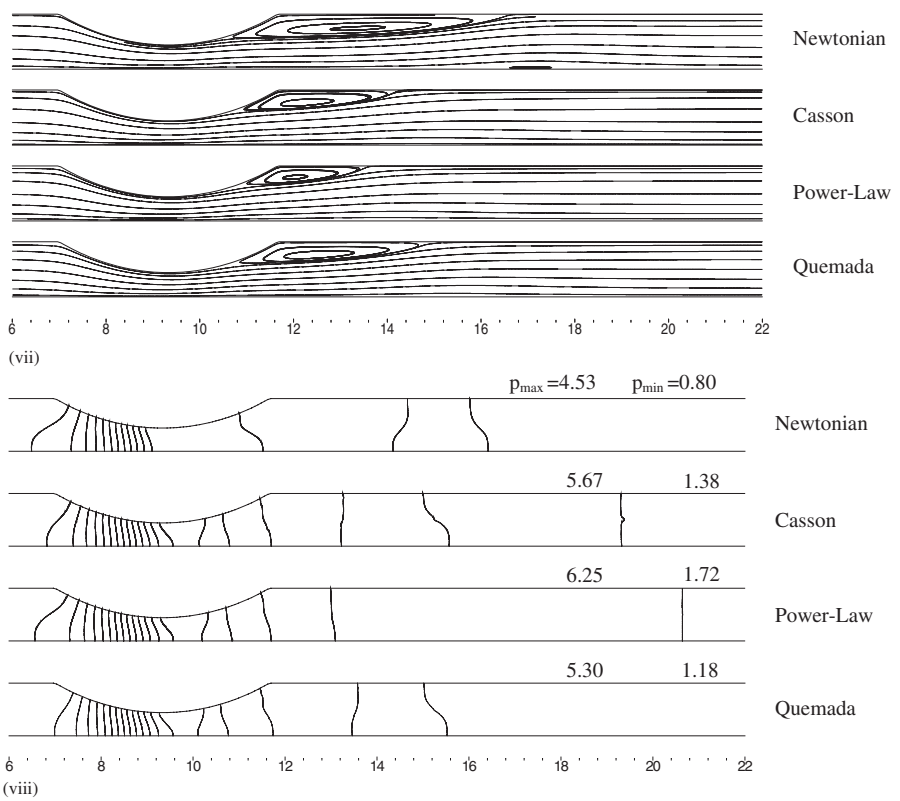

Figure 1. *Continued.*

the no-slip condition. At the outflow boundary, the velocity values at each node $i=N$ are extrapolated from the values at the two inner nodes $i=N-1$ and $i=N-2$, whereas the pressure is set equal to the reference value of 1. At the inflow boundary, the pressure value at each node $i=1$ is derived by linear extrapolation from the values at the two inner nodes $i=2$ and 3, whereas the dimensionless mean inflow velocity $U(t)$ for every time instant throughout the period is

$$\begin{aligned} U(t) &= U_s, && 0 \leqslant t \leqslant \frac{1}{2} \\ U(t) &= U_s - U_p \sin(2\pi t), && \frac{1}{2} < t \leqslant 1 \end{aligned} \tag{39}$$

where t is the dimensionless time (non-dimensionalized with respect to T). The dimensionless values for U_s, (reference velocity) and U_p are 1 and 1.22, respectively.

To specify the inflow velocity for the Newtonian and non-Newtonian flow cases one should write the relation for $U(t)$ in (39) in Fourier series. This expression is the real part of a complex Fourier series

$$U(t) = \text{Real}\left(\sum_{n=0}^{\infty} U_n e^{-2\pi nti}\right) \tag{40}$$

where

$$U_0 = U_s + \frac{U_p}{\pi}, \quad U_1 = -\frac{U_p}{2}\, i, \quad U_n = -\frac{2}{n^2-1}\frac{U_p}{\pi} \quad \text{for } n = 2,4,6,\ldots, \; U_n = 0 \quad \text{for } n = 3,5,7,\ldots \tag{41}$$

and $i = \sqrt{-1}$. The inflow velocity profile should correspond to the fully developed periodic flow in a 2D channel with parallel wall at a distance of $H = 1$. Considering a Newtonian fluid, the dimensionless Navier–Stokes equations are reduced to

$$Str\frac{\partial u}{\partial t} = -\frac{\partial p}{\partial x} + \frac{1}{Re}\frac{\partial^2 u}{\partial y^2} \tag{42}$$

where $u = u(y,t)$ is the velocity profile for which $u(y,t) = u(y,t+1)$ due to the periodicity of the flow. Developing u and p in (42) in a Fourier series expansion and following the rationale used in obtaining the velocity profile for the Poiseuille flow, the time-dependent velocity profile yields

$$u(y,t) = \text{Real}\left(6U_0 y(1-y) + \sum_{n=1}^{\infty} U_n A_n(y) \mathrm{e}^{-2\pi nti}\right) \tag{43}$$

where

$$A_n(y) = \left(1 - \frac{\cosh a_n(y-1/2)}{\cosh a_n/2}\right) \Big/ \left(1 - \frac{2\sinh a_n/2}{a\cosh a_n/2}\right) \tag{44}$$

and $a_n = (1-i)\sqrt{\pi n\, Re\, Str}$.

Equation (43) gives the Newtonian velocity profile for a periodical flow of a known mean inflow-velocity waveform in a channel with parallel walls. This profile is used as an inflow boundary condition for the Newtonian and non-Newtonian cases presented here.

3. NUMERICAL METHOD

The solution of the equations that model the problem is based on the finite-volume scheme [22] with a collocated arrangement of variables in conjunction with the SIMPLE algorithm [23]. The equations are solved through an iterative procedure. Rewriting Equations (1) and (2) in non-dimensional form and omitting the star superscript yields

$$\int_S \mathbf{V}\cdot \mathrm{d}\mathbf{S} = 0 \tag{45}$$

$$Str\frac{\partial}{\partial t}\int_\Omega u\,\mathrm{d}\Omega + \int_S u\mathbf{V}\cdot\mathrm{d}\mathbf{S} = -\int_S p\mathbf{i}_x\cdot\mathrm{d}\mathbf{S} + \int_S \mu\left(\nabla u + \frac{\partial u}{\partial x}\mathbf{i}_x + \frac{\partial v}{\partial x}\mathbf{i}_y\right)\cdot\mathrm{d}\mathbf{S} \tag{46a}$$

$$Str\frac{\partial}{\partial t}\int_\Omega v\,\mathrm{d}\Omega + \int_S v\mathbf{V}\cdot\mathrm{d}\mathbf{S} = -\int_S p\mathbf{i}_y\cdot\mathrm{d}\mathbf{S} + \int_S \mu\left(\nabla v + \frac{\partial u}{\partial y}\mathbf{i}_x + \frac{\partial v}{\partial y}\mathbf{i}_y\right)\cdot\mathrm{d}\mathbf{S} \tag{46b}$$

The discretization method will be analysed for the continuity equation (45) and the x-momentum equation (46a) whereas the analysis for (46b) is similar. For the discretization

of the unsteady term on the control volume (CV) with centre P (Figure 1(ii)) a first-order scheme is introduced, thus

$$\frac{\partial}{\partial t}\int_{\Omega} u\,\mathrm{d}\Omega \approx \frac{\Delta\Omega}{\Delta t}(u_P - u_P^n) \tag{47}$$

For the discretization of the other terms in (46a) the surface integrals may be split into four CV face integrals. Attention will be focused on face 'e' (Figure 1(ii)) and the other faces are assumed to be treated in the same way. In discretizing the convection term, the mass flux through face 'e' is evaluated using existing known velocity

$$\dot{m}_e^m = \int_{S_e} \mathbf{V}\cdot\mathrm{d}\mathbf{S} \approx u_e^{m-1} S_e \tag{48}$$

where u_e^{m-1} can be calculated by linear interpolation between u_P^{m-1} and u_E^{m-1}; m and $m-1$ denote the current and previous iterations, respectively. Hence, the convection term becomes

$$\int_{S_e} u\mathbf{V}\cdot\mathrm{d}\mathbf{S} \approx \dot{m}_e u_e \tag{49}$$

The value of u_e can be calculated using either an upwind difference scheme (UDS) or a central difference scheme (CDS). The UDS yields

$$u_e = \begin{cases} u_P & \text{if } (\mathbf{V}\cdot\mathbf{S})_e > 0 \\ u_E & \text{if } (\mathbf{V}\cdot\mathbf{S})_e < 0 \end{cases} \tag{50}$$

and the CDS yields

$$u_e = u_E l_e + u_P(1 - l_e) \tag{51}$$

where

$$l_e = \frac{x_e - x_P}{x_E - x_P} \tag{52}$$

For better numerical convergence, a combination of the aforementioned schemes is used. This is known as the deferred correction approach, that is

$$\int_{S_e} u\mathbf{V}\cdot\mathrm{d}\mathbf{S} \approx \dot{m}_e u_e^{\mathrm{UDS}} + \dot{m}_e(u_e^{\mathrm{CDS}} - u_e^{\mathrm{UDS}})^{m-1} \tag{53}$$

where the superscripts CDS and UDS denote approximation by central and upwind differences, respectively. The term in brackets is evaluated using values from the previous iteration while the matrix of the unknown variables is computed using the UDS approximation.

Calculation of the diffusive term requires evaluation of the stresses τ_{xx} and τ_{xy} on the CV faces 'e' and 'n', respectively. CD approximation leads to

$$\begin{aligned}\int_{S_{e,n}} \mu\left(\nabla u + \frac{\partial u}{\partial x}\mathbf{i}_x + \frac{\partial v}{\partial x}\mathbf{i}_y\right)\cdot\mathrm{d}\mathbf{S} &= 2\left(\mu\frac{\partial u}{\partial x}\right)_e S_e + \left(\mu\frac{\partial v}{\partial x} + \mu\frac{\partial u}{\partial y}\right)_n S_n \\ &\approx \mu_e\frac{u_E - u_P}{x_E - x_P}S_e + \mu_n\frac{u_N - u_P}{x_N - x_P}S_n + \left(\mu_e\frac{u_E - u_P}{x_E - x_P}S_e + \mu_n\frac{v_{ne} - v_{nw}}{x_{ne} - x_{nw}}S_n\right)^{m-1}\end{aligned} \tag{54}$$

where $S_n = x_{ne} - x_{nw}$ and $S_e = y_{ne} - y_{se}$. The values of μ_e and μ_n are calculated from (12) using the values of u and v from the previous iteration. The term $v_{ne} - v_{sw}$ is calculated by linear interpolation from the corresponding values at the surrounding nodes.

The pressure term of the x-momentum equation corresponding to the whole CV is discretized as

$$-\int_S p\mathbf{i}_x \cdot \mathrm{d}\mathbf{S} \approx -(p_e S_e - p_w S_w)^{m-1} \tag{55}$$

where p_e^{m-1} and p_w^{m-1} can be calculated by linear interpolation between p_P^{m-1} and p_E^{m-1}, and between p_P^{m-1} and p_W^{m-1}, respectively.

If the aforementioned approximations are substituted into (46a) the following algebraic equation is obtained:

$$A_P^x u_P + \sum_i A_i^x u_i = Q_P^x, \quad i = E, W, N, S \tag{56}$$

where A_i are the coefficients of the unknowns and Q_P are the source terms containing all known terms arising from the discretization.

The coefficients for the y-momentum equation (46b) are obtained in a similar fashion yielding a discretized equation similar to (56):

$$A_P^y v_P + \sum_i A_i^y v_i = Q_P^y, \quad i = E, W, N, S \tag{57}$$

For solving the flow and pressure field the SIMPLE method is applied. In the first step of the method a pressure-(p^{m-1}) and a velocity field (u^{m-1}, v^{m-1}) are guessed. Then the discretized momentum equations (56) and (57) are solved using the guessed field to yield the velocity components u^*, v^*. These values do not generally satisfy mass conservation on each CV. Therefore, the velocities u^* and v^* need to be corrected as follows:

$$u^m = u^* + u', \quad v^m = v^* + v' \tag{58}$$

and the final values in the m iteration should also satisfy the momentum equation. This is possible only if the pressure also is corrected:

$$p^m = p^{m-1} + p' \tag{59}$$

Expressing the velocity on cell face e in terms of the momentum equation one can obtain two equations for each of u^* and u^m. Subtracting these equations yields

$$u'_e = B_e - C_e(p'_E - p'_P)S_e \tag{60}$$

where B_e is a term that includes velocity correction terms on other nodes whereas C_e accounts for geometric properties of the current CV. The corrected velocities are required to satisfy the continuity equation. If the mass flux through cell face 'e' is

$$\dot{m}_e = u_e^m S_e = (u_e^* + u'_e)S_e \tag{61}$$

then similar expression for the rest of the CV faces yields

$$\sum_c \dot{m}_c = \Delta\dot{m}^* + \Delta\dot{m}' = 0, \quad c = e, w, n, s \tag{62}$$

Substituting the term $\Delta\dot{m}'$ in (62) as in (60) yields

$$A_P p'_P + \sum_i A_i p'_i = -\Delta\dot{m}^* - \sum_c B_c, \quad i = E, W, N, S, \quad c = e, w, n, s \tag{63}$$

where A are the coefficients of the unknown variables resulting from the discretized expressions for the pressure corrections. If the last terms on the right-hand side (RHS) of (63) are omitted because they involve the velocity corrections, which are not yet known, one obtains the *pressure-correction equation*

$$A_P p'_P + \sum_i A_i p'_i = -\Delta\dot{m}^*, \quad i = E, W, N, S \tag{64}$$

Applying (64) on all CVs of the domain results to a system of equations, the solutions of which gives the pressure corrections on each computational node. These are used further to correct the velocity values, which will now satisfy the continuity equations. However, they do not satisfy the momentum equations, so another iteration must be performed using the solutions from the previous time step as an initial guess. This iteration procedure continues until reaching the desired accuracy. It should be noted that if the last term on the RHS of (63) is neglected the SIMPLE algorithm may lead to divergence and therefore underrelaxation should be used. The solution of the systems of equations (56), (57) and (64) is carried out using Stone's method [24].

4. RESULTS AND DISCUSSION

4.1. Preliminary remarks

In stenotic flows, of particular interest are the phenomena of the vortex generation and propagation as well as the distribution of the wall shear stress (WSS). These are considered the most prominent attributes for blood flows because of their relation to atheroma formation in arteries. To study these phenomena, we have considered three different flow cases. The first case concerns steady and the other two unsteady flows. For Newtonian flow in all cases the value of the Reynolds number used in the calculations is $Re = 360$ as in the work by Rosenfeld [4, 5]. Additional parameters should be defined for non-Newtonian models, and their values were chosen according to measurements by Spiller *et al.* [25] pertinent to stenotic arteries. These are $Re_{\mathrm{CA}} = 360$, $Bi = 0.675$ for the Casson model, $Re_{\mathrm{PL}} = 110$ for the power-law model and $Re_{QU} = 931$, $\gamma_c^* = 0.364$ for the Quemada model. The above values have been chosen under the assumption that the inflow rate or the mean inflow velocity is the same for computations based on different models. Choosing the same value for both Re and Re_{CA} implies that for the Newtonian case the viscosity μ corresponds to μ_∞ of the Casson model. The difference between the two unsteady cases is the value of the Strouhal number; $Str = 0.05$ and 0.368 have been used. The higher Strouhal number has been chosen because comparisons with the corresponding results of Rosenfeld [4, 5] can be obtained. The use of different Strouhal numbers is analogous to the change from normal to tachycardial conditions.

Three grids were tested namely 225×50, 450×100 and 900×150. The grid spacing was uniform in both x and y directions. From the dimensionless WSS distribution on the upper wall for a steady Newtonian flow with $Re = 360$ (Figure 1(iii)), it can be seen that grid independence is achieved for a 450×100 grid. Therefore, this grid was used in all computations

conducted in the present study. Another important aspect is the length of the downstream segment L_d (Figure 1(i)), which should be long enough to allow a fully developed flow at the outlet. Downstream of the stenosis, the flow variations extend longer for the unsteady Newtonian flow with $Re = 360$ and $Str = 0.05$, at $t/T = 0.2$. For this flow case the value of $L_d = 28.34$ was found sufficient for the velocity profile to regain its fully developed attributes at the outlet boundary (Figure 1(iv)). For the unsteady cases it is also important that the results converge in time, i.e. they remain the same (based on an accuracy threshold 10^{-8} for double precision calculations) between two consecutive unsteady cycles. Calculations were carried out for several cycles and converged solution was obtained after six cycles. This was verified by comparing the upper wall WSS distribution in two consecutive cycles at $t/T = 0.2$ for the Newtonian flow with $Re = 360$ and $Str = 0.368$ (Figure 1(v)). The present results were compared (Figure 1(vi)) with the experimental and numerical results of Rosenfeld [5] and Park [26], respectively, with respect to the streamwise location of the centre of the B1 vortex throughout the cycle (see 4.3.1(i) and Figure 2(ii) for nomenclature of vortices). The comparison with the experiment [2, 6] concerns the Newtonian case with $Re = 180$ and $Str = 0.368$, while the comparison with the numerical results of Rosenfeld [5] has been obtained for the same Strouhal number and $Re = 360$. The present results are in a close agreement with both the aforementioned previous numerical data and experiments (Figure 1(vi)) thus eliminating any numerical uncertainty.

4.2. Steady case

Prior to examining the unsteady cases an initial investigation was carried out for steady stenotic flow using all models. For the Newtonian model the Reynolds number is $Re = 360$, while the parameters for the non-Newtonian models are obtained as described in Section 2.3, i.e. in terms of the same inflow rate with the Newtonian flow case.

The streamlines for all the models are shown in Figure 1(vii). In all cases, upstream of the stenosis no eddy is formed and the flow proceeds smoothly to the constriction. On the lee of the stenosis a stationary eddy is formed, the size of which is different for every model. For the Newtonian case this eddy is the largest in size, while a second smaller eddy on the opposite wall is also generated. In the flow field of the non-Newtonian models the eddy downstream of the constriction is smaller than the Newtonian case and the second eddy is absent. The eddy for the Quemada model is the largest with a small difference from the eddy for the Casson model, while the eddy for the power-law model is the smallest one. The difference in size of the eddy for each of the models can be explained from the fact that for this case, the behaviour of the power-law model is the most viscous followed in order of decreasing viscous behaviour by the Casson, the Quemada and finally the Newtonian model.

The dimensionless pressure distribution for every model is shown in Figure 1(viii). In this figure, the maximum and minimum dimensionless pressure values are also shown and between these values 15 contours have been plotted. It can be seen that every model exhibits similar patterns, which can be analysed in three parts. In the first part the flow is far upstream, still undisturbed and therefore the pressure drop is uniform. In the second part the flow is within the stenosis area where the pressure drops rapidly as the flow enters the constriction and reaches its minimum value at a point slightly further from the minimum constriction width. The pressure increases as the flow exits the stenosis. In the third part the flow is sufficiently far downstream of the stenosis and has therefore regained its fully developed attributes and

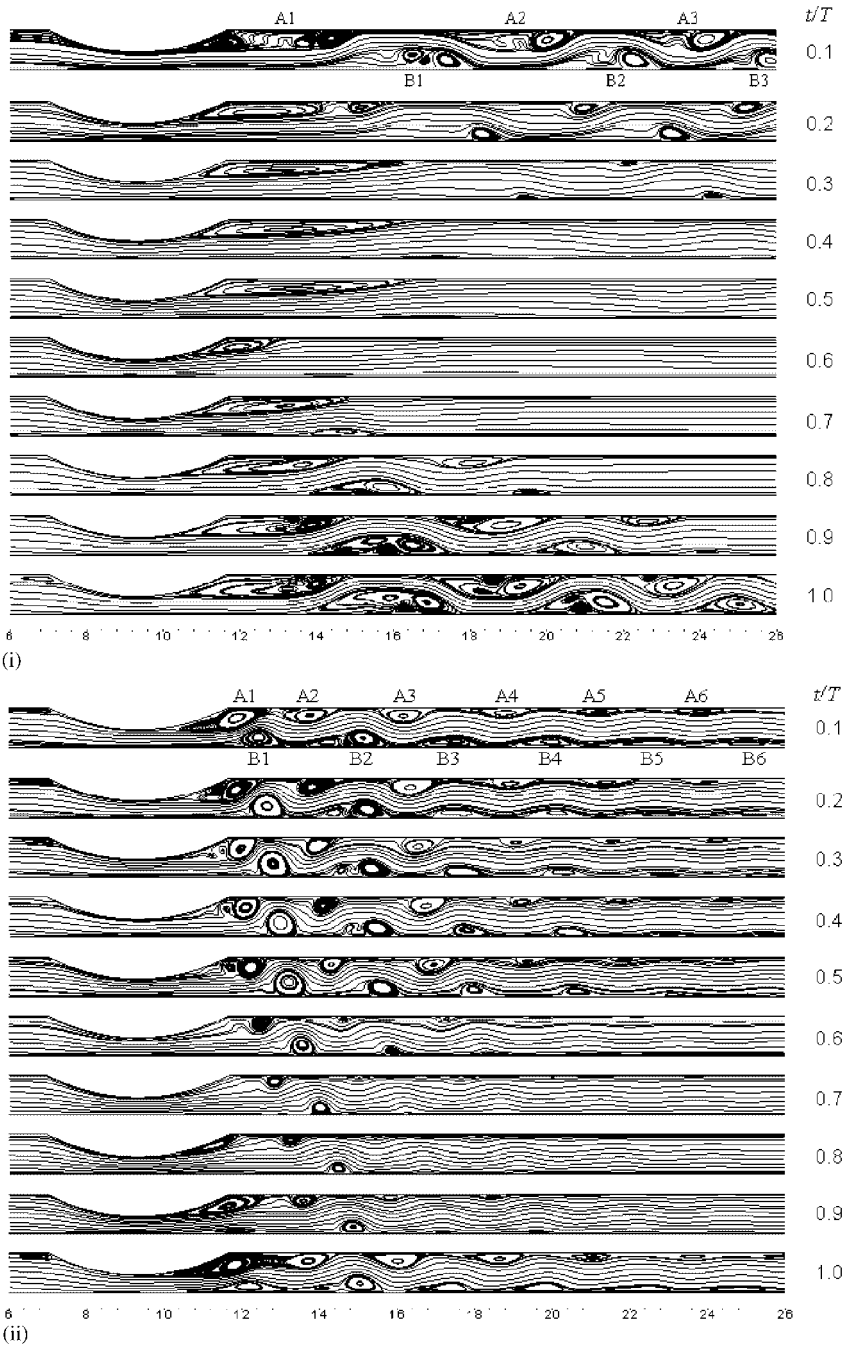

Figure 2. Instantaneous streamlines for a Newtonian fluid at $Re = 360$, at selected instants. (i) $Str = 0.05$. (ii) $Str = 0.368$.

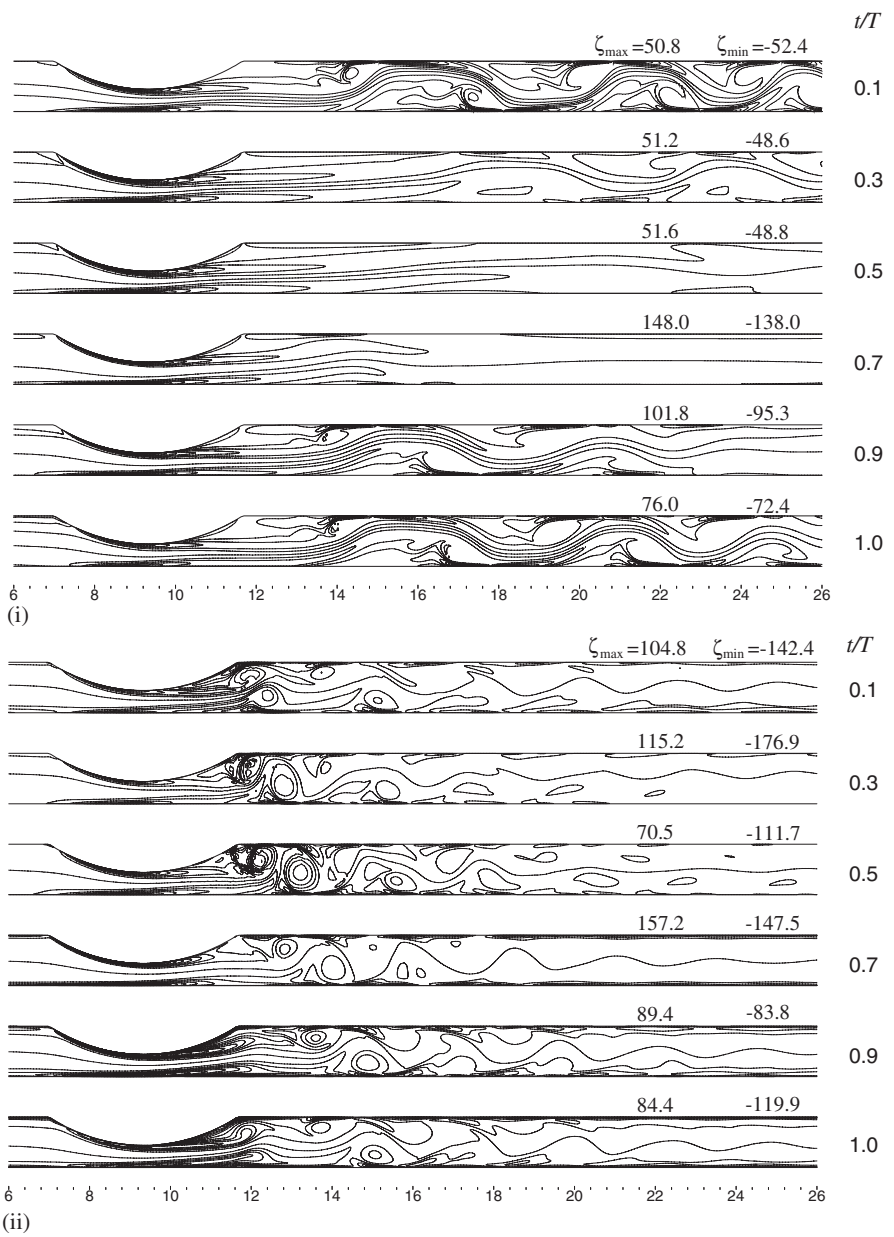

Figure 3. Instantaneous vorticity distribution for a Newtonian fluid at $Re = 360$, at selected time instants. (i) $Str = 0.05$. (ii) $Str = 0.368$.

therefore it drops uniformly again. Considering that the dimensionless pressure at the outlet is equal to 1 for every model case, then the highest dimensionless pressure upstream appears in the power-law case and becomes lower (in decreasing order) in the cases of the Casson, Quemada and Newtonian models.

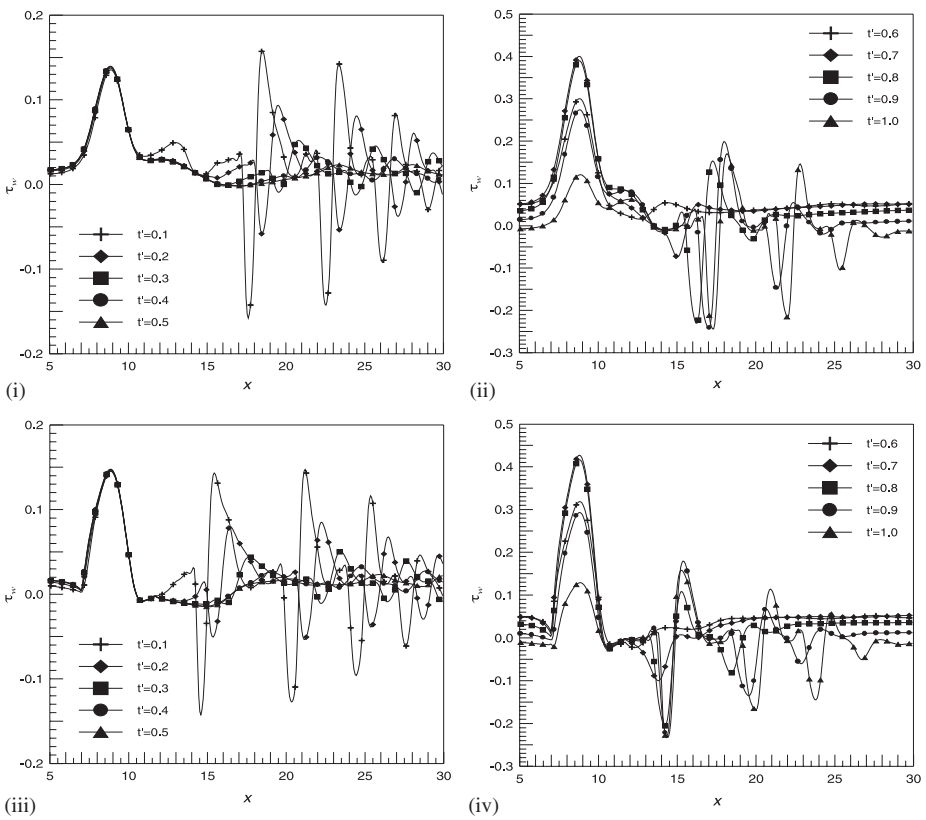

Figure 4. Dimensionless shear stress distribution for a Newtonian fluid at $Re = 360$, at selected time instants. (i) Lower wall, $t' = 0.1$–0.5, $Str = 0.05$. (ii) Lower wall, $t' = 0.6$–1.0, $Str = 0.05$. (iii) Upper wall, $t' = 0.1$–0.5, $Str = 0.05$. (iv) Upper wall, $t' = 0.6$–1.0, $Str = 0.05$. (v) Lower wall, $t' = 0.1$–0.5, $Str = 0.368$. (vi) Lower wall, $t' = 0.6$–1.0, $Str = 0.368$. (vii) Upper wall, $t' = 0.1$–0.5, $Str = 0.368$. (viii) Upper wall, $t' = 0.6$–1.0, $Str = 0.368$.

4.3. *Unsteady cases*

4.3.1. Flow field. (i) $Str = 0.05$: For the $Str = 0.05$ case, the streamline patterns are shown in Figures 2(i), 5(i), 8(i) and 11(i) for the Newtonian, Casson, power-law and Quemada models, respectively. The streamline patterns are shown for ten equally spaced time instants of the period. Some general flow phenomena occur for all models and will be described for the Newtonian case (Figure 2(i)).

At the beginning of the new period, the flow field has a complicated structure in which two series of eddies on the upper and lower walls are prominent ($t' = 0.1$). The core flow is wavy and beneath and above the waves' crests and troughs, eddies are located. For the sake of reference, starting from the lee of the constriction, the first region above a trough is named '$A1$', the second '$A2$' and so on. In the same manner, the first region beneath a crest on the lower wall is named '$B1$', the second '$B2$' and so on. Caution must be exercised in

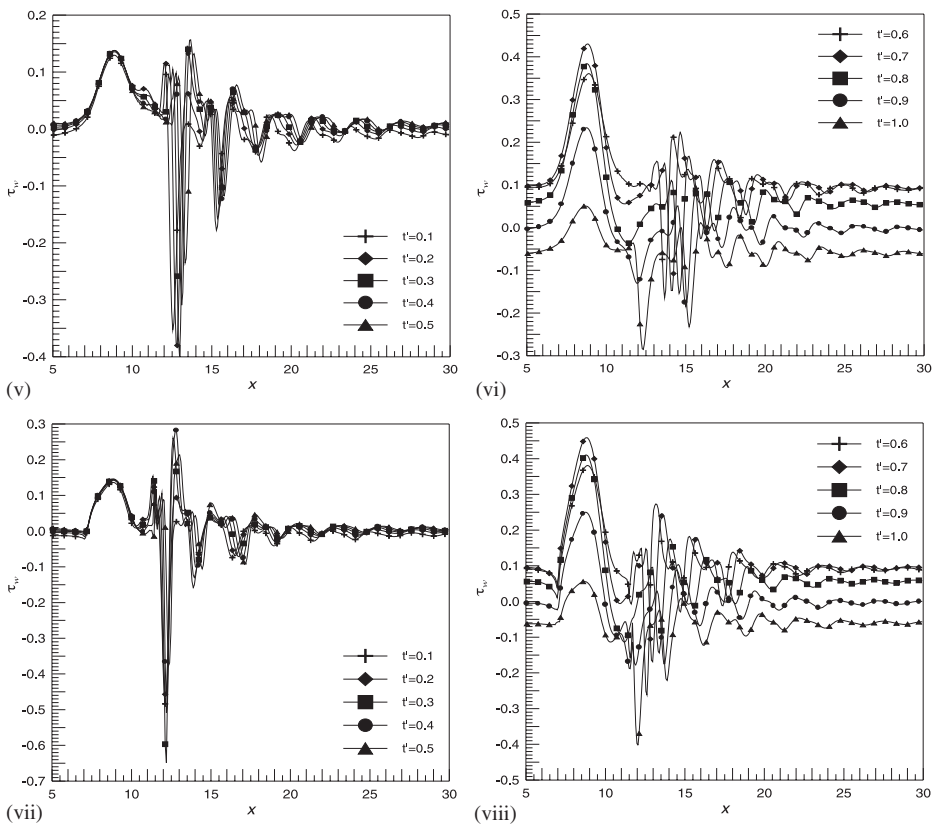

Figure 4. *Continued.*

naming eddies in this way, however, since an eddy named '$A1$' for example, may be named '$A2$' after a while because of a new eddy forming upstream. Although at this stage, which is the first half of the period, the inflow rate is steady, the streamline patterns progressively change owing to the accumulation of transient effects from the second half of the previous cycle. At $t' = 0.2$ the eddy in the lee of the constriction becomes more elongated and the rest of the eddies move downstream and become weaker ($t' = 0.2$–0.3). At the end of the first half ($t' = 0.5$) the flow seems to be stabilizing. Most eddies have vanished except the eddy in the lee of the constriction, the size of which no more alters, and another small eddy at the opposite wall. As the acceleration phase starts, the core flow is straightened out and the eddy in the lee of the constriction becomes smaller in size ($t' = 0.6$). In addition, the eddy in the lee of the constriction becomes further elongated and the eddy on the opposite wall reappears ($t' = 0.7$). As the deceleration phase starts, the core flow becomes more wavy and more eddies form, while in the region $B1$ the eddy-doubling phenomenon occurs: beneath one crest, two counter-rotating eddies form ($t' = 0.8$). As the deceleration progresses, the width of the core flow decreases and the eddy-doubling phenomenon occurs for all eddies ($t' = 0.9$–1.0). In addition, the large eddies break into two co-rotating parts that coexist above or under a trough or crest, as in region A2 for $t' = 1.0$. As can be seen in $B1$ for $t' = 1.0$,

the second co-rotating eddy has initiated another eddy-doubling phenomenon resulting in the co-existence of four eddies underneath the same crest. All eddies tend to grow larger in size and propagate downstream during this phase.

In the aforementioned flow phases, the phenomena associated with the non-Newtonian models are different from those in the Newtonian case. For the Casson model (Figure 5(i)) at $t' = 0.1$, the only region that accommodates two eddies is $A1$, downstream of which one eddy occurs beneath or above a trough or a crest. Eddies are becoming rapidly weaker ($t' = 0.2$) and subsequently one stabilized, elongated eddy prevails ($t' = 0.3$) the size of which remains unchanged throughout the steady phase. The only difference between the patterns for the remaining of the steady phase ($t' = 0.3–0.5$) is that the flow is still wavy at $t' = 0.1$, but not to the extent that it allows further eddy forming. The stationary eddy is very much smaller than in the corresponding Newtonian case and no second eddy ($B1$) exists. The patterns at the beginning of the acceleration phase ($t' = 0.6–0.7$) are quite similar to the Newtonian flow patterns. Advancing to $t' = 0.8$ there is no eddy-forming phenomenon in $B1$ and $B2$ does not exist. This phenomenon does not appear at any of the following time instants and eddy-breaking appears only for $A1$ and $B1$ at $t' = 1.0$. During this phase, deceleration causes more eddies to form but their size is substantially smaller than in the Newtonian case.

In the case of the power-law model (Figure 8(i)), at the beginning of the steady phase ($t' = 0.1$) the behaviour seems more viscous than in the aforementioned cases. Region $A3$ is barely formed whereas $B3$ is absent. These eddies dissipate faster than in the previous cases and by $t' = 0.2$ only $A1$ exists. The flow is wavy but progressively straightens until the end of the steady phase ($t' = 0.5$). At the acceleration phase ($t' = 0.6–0.7$), eddy $A1$ is small but becomes progressively larger and $B1$ is formed similarly as in the previous cases. At the deceleration phase, $A2$ is formed ($t' = 0.8$) as in the previous cases, but during the rest of the phase, eddy forming is restricted to $A2$ and $B2$ at $t' = 0.9$ and 1.0, respectively. Eddies become stronger at the end of the phase, but no eddy-doubling phenomenon or even eddy-breaking is evident.

In the case of the Quemada model (Figures 5(i)–11(i), at the beginning of the steady phase ($t' = 0.1$) the phenomena from the previous cycle are still intense. Next, at $t' = 0.2$, the size of the eddies is between the corresponding sizes in the Newtonian and Casson cases. Further into the steady phase, all eddies except $A1$ dissipate, as in the Casson case, but as the flow stabilizes $A1$ is longer than in the Casson case. At the deceleration phase, eddy forming is similar to the Casson case. The only difference is that the eddy-doubling phenomenon is evident here ($B1$ at $t' = 0.9–1.0$) and eddy breaking occurs sooner ($t' = 0.9$).

(ii) $Str = 0.368$: For $Str = 0.368$ case, the streamline patterns are shown in Figures 2(ii), 5(ii), 8(ii) and 11(ii) for the Newtonian, Casson, power-law and Quemada models, respectively. The general phenomena that occur for all models will be described for the Newtonian model (Figure 2)(ii)). During the steady phase ($t' = 0.1–0.5$) the flow field is highly disturbed and alters throughout the phase, despite the steady inflow conditions. This is due to the accumulation of transient effects from the second half of the previous cycle, which are more intense than for $Str = 0.05$. The series of eddies on the upper and lower walls propagate progressively downstream as the far downstream eddies reduce in size. Eddy doubling is evident, especially for eddy $A1$ and the eddy-breaking phenomenon also occurs. As the acceleration phase starts ($t' = 0.6$) the far downstream eddies disappear and the rest become smaller in size. Later ($t' = 0.7$) only two eddies remain, one on each wall. At the beginning of the deceleration phase ($t' = 0.8$) a new eddy forms in the lee of the constriction as the

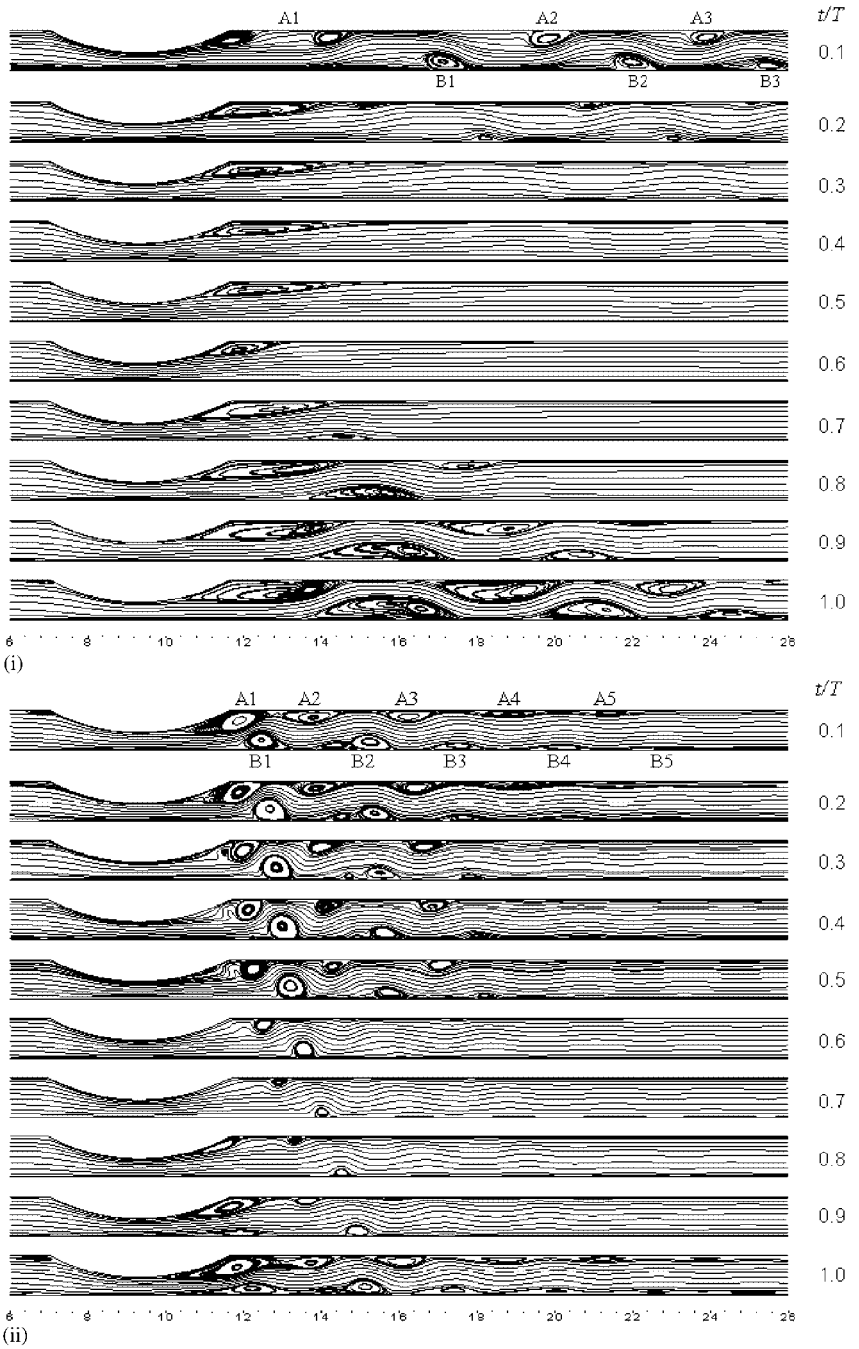

Figure 5. Instantaneous streamlines for a Casson fluid at $Re_{CA} = 360$, $Bi = 0.675$, at selected time instants. (i) $Str = 0.05$. (ii) $Str = 0.368$.

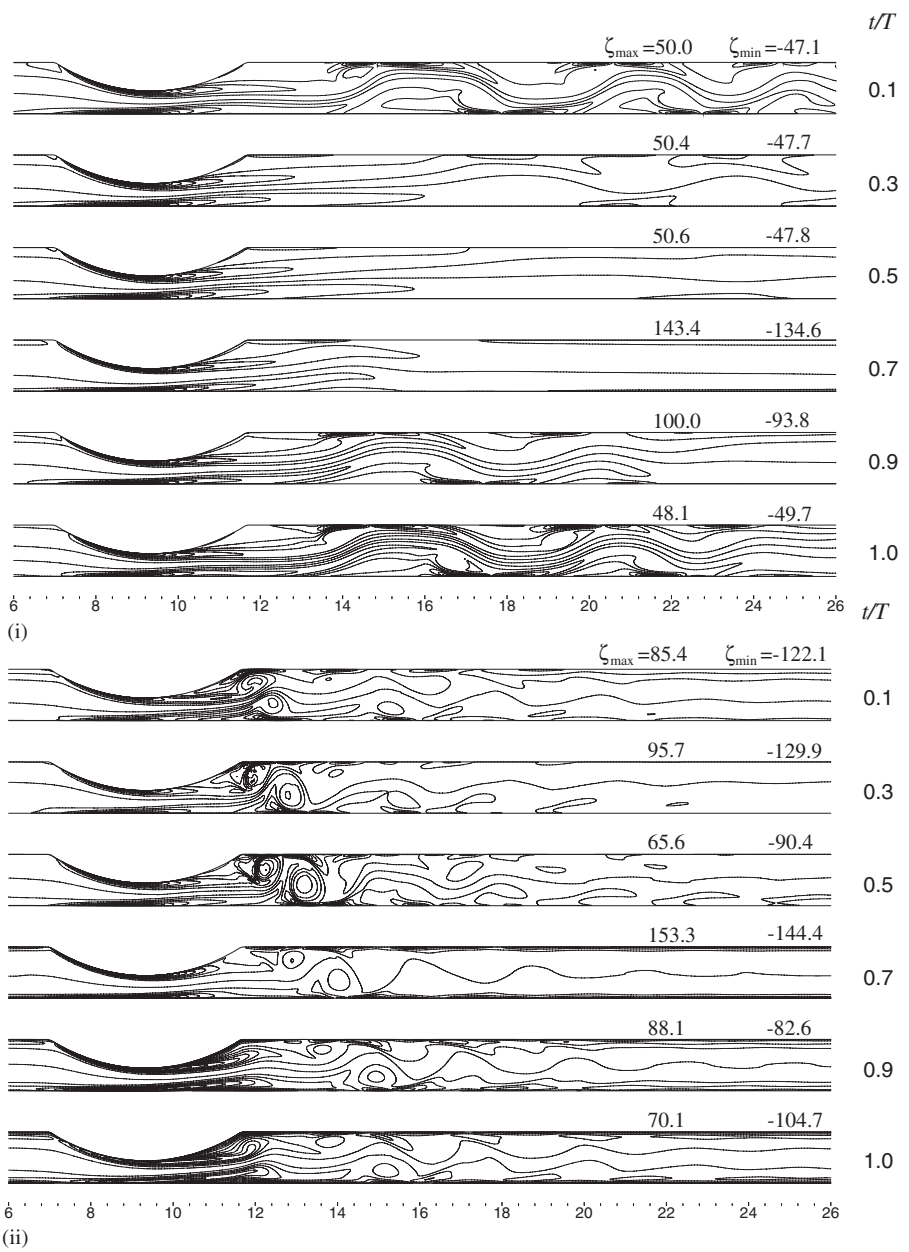

Figure 6. Instantaneous vorticity distribution for a Casson fluid at $Re_{CA} = 360$, $Bi = 0.675$, at selected time instants. (i) $Str = 0.05$. (ii) $Str = 0.368$.

existing ones move downstream. As the deceleration proceeds ($t' = 0.9$), more eddies form downstream and the core flow becomes more wavy. Another eddy also forms opposite $A1$. At the end of the deceleration phase ($t' = 1.0$) the core flow region is narrower and a series of

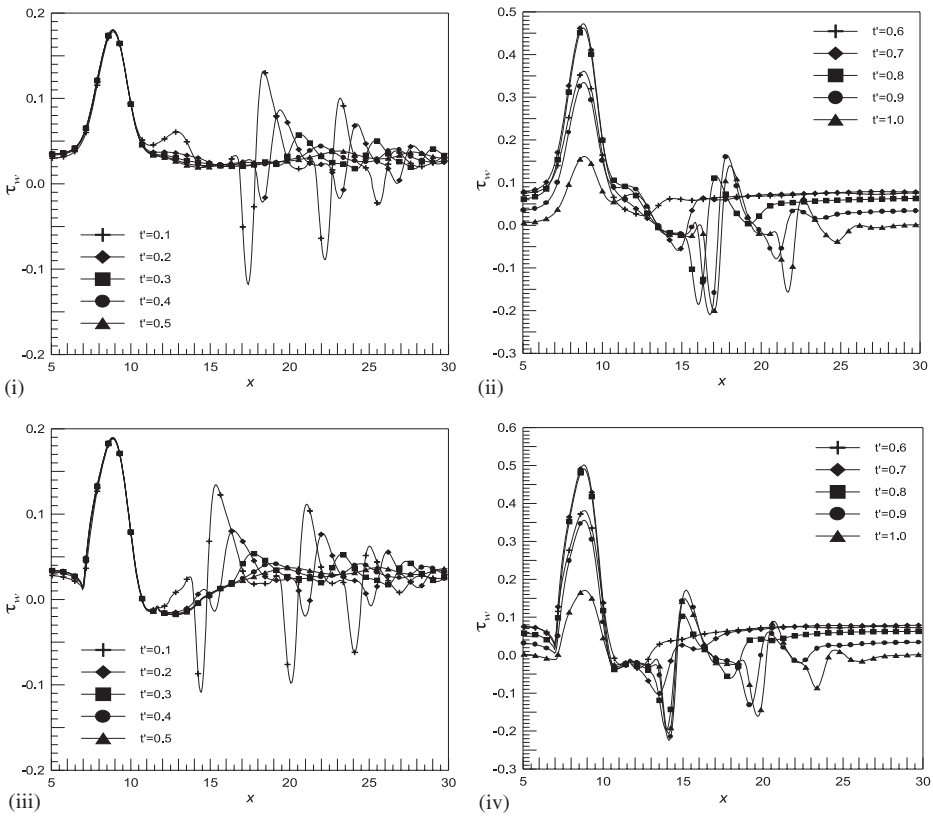

Figure 7. Dimensionless shear stress distribution for a Casson fluid at $Re_{CA} = 360$, $Bi = 0.675$, at selected time instants. (i) Lower wall, $t' = 0.1$–0.5, $Str = 0.05$. (ii) Lower wall, $t' = 0.6$–1.0, $Str = 0.05$. (iii) Upper wall, $t' = 0.1$–0.5, $Str = 0.05$. (iv) Upper wall, $t' = 0.6$–1.0, $Str = 0.05$. (v) Lower wall, $t' = 0.1$–0.5, $Str = 0.368$. (vi) Lower wall, $t' = 0.6$–1.0, $Str = 0.368$. (vii) Upper wall, $t' = 0.1$–0.5, $Str = 0.368$. (viii) Upper wall, $t' = 0.6$–1.0, $Str = 0.368$.

eddies form on both walls. Eddy breaking occurs for eddy $B2$ and eddy doubling is initiated for both $A2$ and $B2$ in the Newtonian case; this is more evident at $t' = 0.1$.

For the Casson case (Figure 5(ii)) at the beginning of the steady phase ($t' = 0.1$) the downstream eddies are fewer and less intense compared to the Newtonian case, and eddy doubling for $A2$ is absent. At $t' = 0.2$ the eddy regions reduce to four on the upper wall and three on the lower wall. For the rest of the phase ($t' = 0.3$–0.5) three eddy regions at each wall exist in contrast to the Newtonian case where all eddies from the beginning of the phase exist till the end, though they are smaller in size. At the beginning of the acceleration phase ($t' = 0.6$) only two eddies, one on each wall, are evident and reduce in size progressively ($t' = 0.7$). At the beginning of the deceleration phase ($t' = 0.8$) the flow patterns are similar to the Newtonian case whereas later ($t' = 0.9$) the eddy generation is less intense with only two new eddies, $B1$ and $A3$, being formed. At the end of the deceleration phase, the patterns are again similar to the Newtonian case but the eddies downstream are weaker.

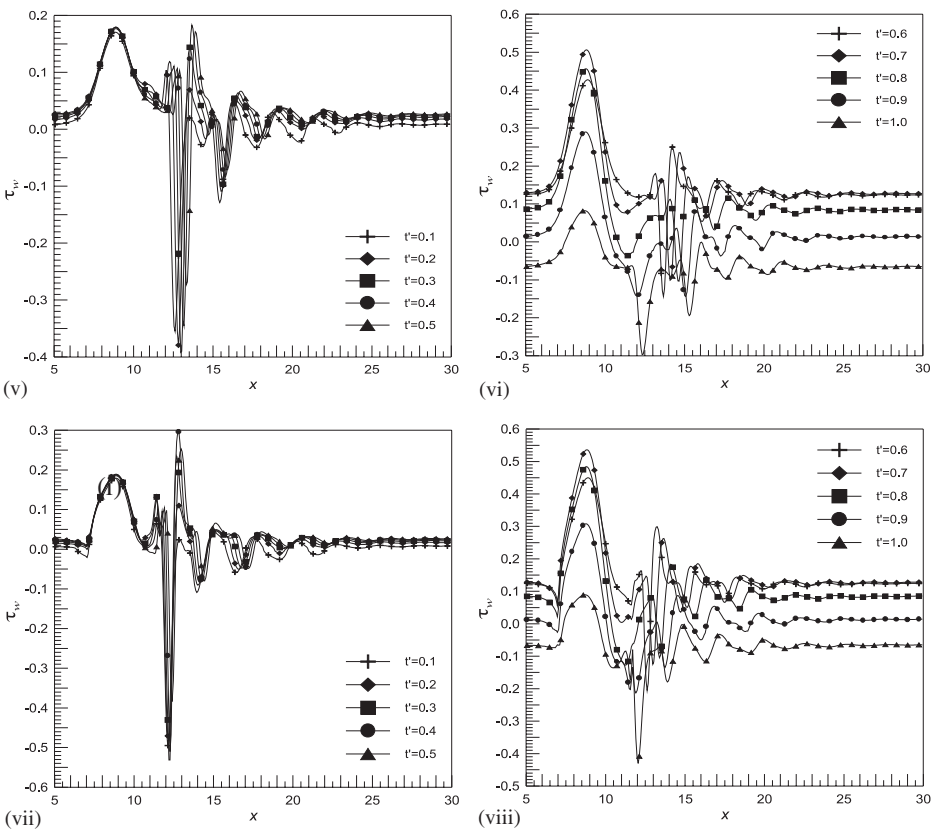

Figure 7. *Continued.*

In the case of the power-law model (Figure 8(ii)) at the beginning of the steady phase ($t' = 0.1$), as in the Casson case, no eddy doubling is evident. The downstream eddies are weaker and fewer than in either the Newtonian or the Casson case. Eddy areas reduce to three only on the upper and two on the lower wall for $t' = 0.2$, and remain so until the end of the steady phase. At the beginning of the acceleration phase ($t' = 0.6$) the eddies are reduced to one at each wall, as in the Casson case, and become progressively weaker ($t' = 0.7$). At the beginning of the deceleration phase ($t' = 0.8$) only $A1$ in the lee of the constriction is formed, as in the Newtonian and Casson cases, but later at $t' = 0.9$ only $B1$, additionally, forms and eddy forming does not occur downstream of the already existing eddies. At the end of the deceleration phase ($t' = 1.0$) the patterns are similar to those in the Casson case with intense eddy formation downstream while eddies are weaker than for the Newtonian case.

In the case of the Quemada model (Figure 11(ii)), at the beginning of the steady phase ($t' = 0.1$) the flow is highly disturbed with a series of eddies on each wall. The patterns are similar to the Casson case where eddy doubling is evident in $B2$, but not in $A2$. Progressively the eddies become fewer, owing to their dissipation far downstream, reducing to three only on each wall by the end of the phase ($t' = 0.5$). The secondary eddy at $A1$, resulting from eddy

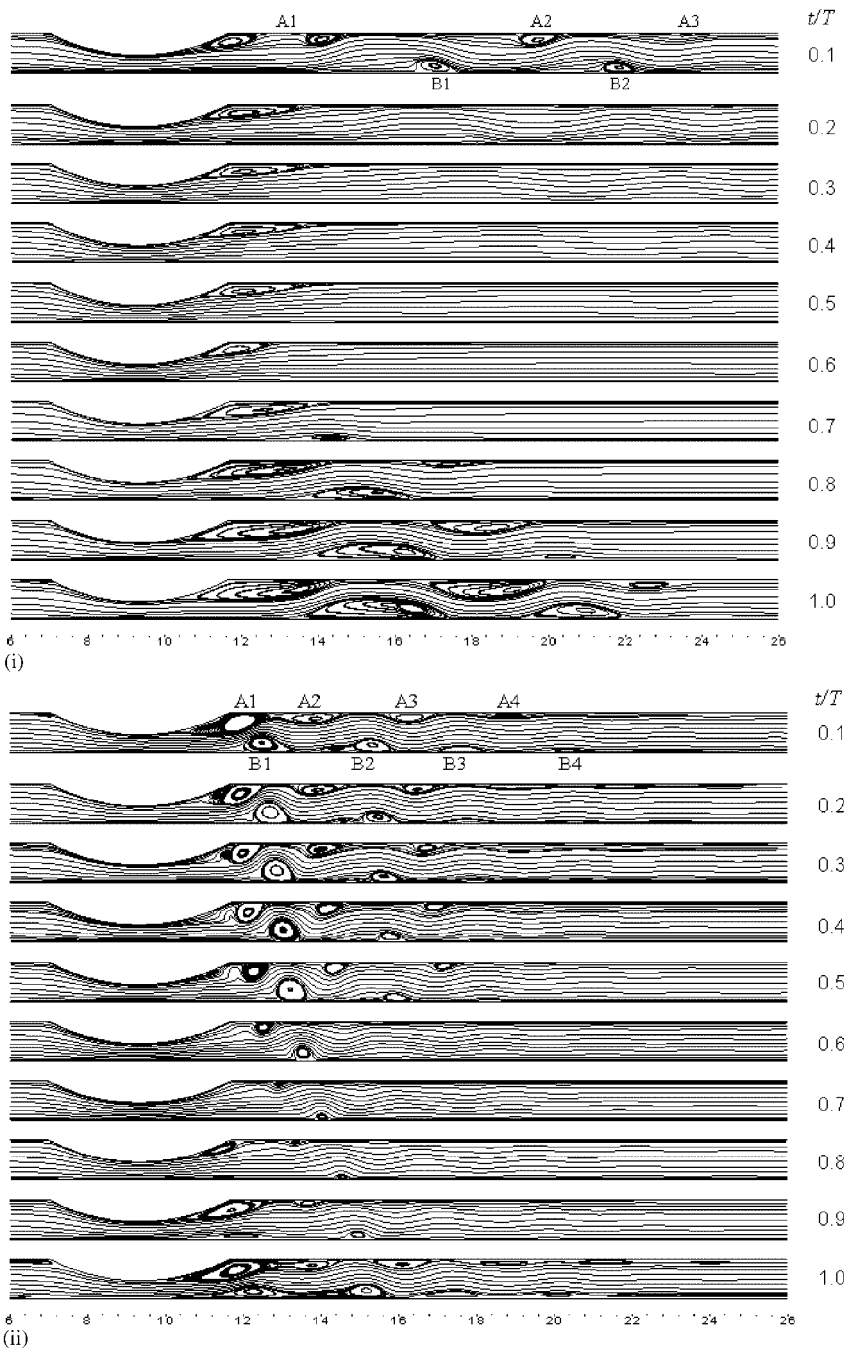

Figure 8. Instantaneous streamlines for a power-law fluid at $Re_{PL} = 110$, at selected time instants. (i) $Str = 0.05$. (ii) $Str = 0.368$.

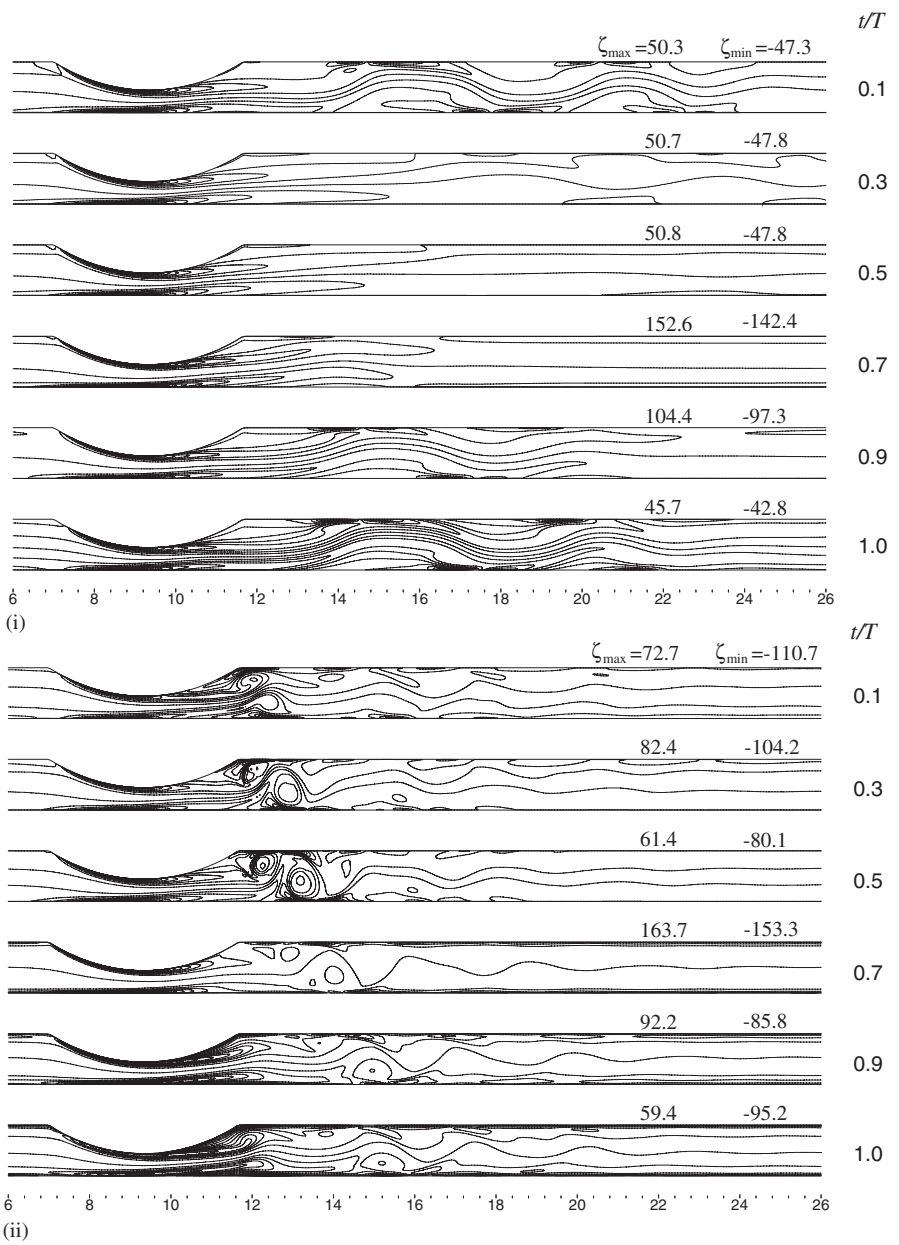

Figure 9. Instantaneous vorticity distribution for a power-law fluid at $Re_{PL} = 110$, at selected time instants. (i) $Str = 0.05$. (ii) $Str = 0.368$.

doubling at the beginning of the steady phase, is still evident at the end of the phase, unlike the rest of the non-Newtonian models. At the beginning of the acceleration phase ($t' = 0.6$) only two eddies are evident, which progressively reduce in size ($t' = 0.7$) just as in the rest

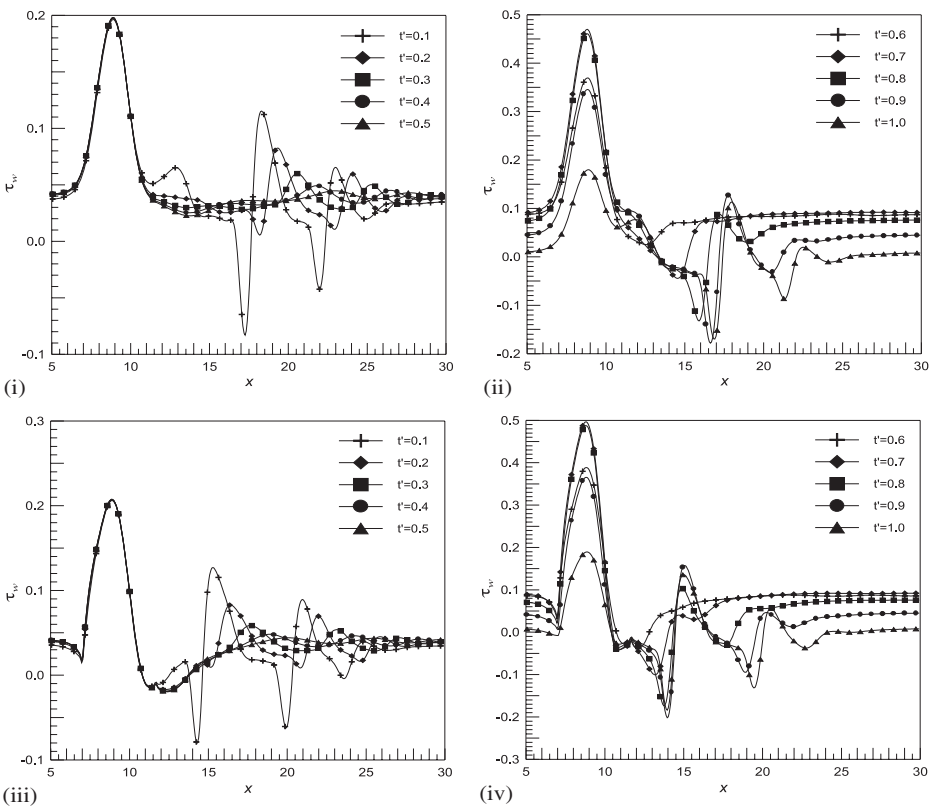

Figure 10. Dimensionless shear stress distribution for a power-law fluid at $Re_{PL} = 110$, at selected time instants. (i) Lower wall, $t' = 0.1$–0.5, $Str = 0.05$. (ii) Lower wall, $t' = 0.6$–1.0, $Str = 0.05$. (iii) Upper wall, $t' = 0.1$–0.5, $Str = 0.05$. (iv) Upper wall, $t' = 0.6$–1.0, $Str = 0.05$. (v) Lower wall, $t' = 0.1$–0.5, $Str = 0.368$. (vi) Lower wall, $t' = 0.6$–1.0, $Str = 0.368$. (vii) Upper wall, $t' = 0.1$–0.5, $Str = 0.368$. (viii) Upper wall, $t' = 0.6$–1.0, $Str = 0.368$.

of the non-Newtonian cases. At the beginning of the deceleration phase ($t' = 0.8$) $A1$ forms, followed by $B1$, $B3$ and $A3$ at $t' = 0.9$. This is similar to the Casson case, considering that $B3$ barely forms. At the end of the deceleration phase ($t' = 1.0$) a series of eddies on the upper and lower walls is formed. The flow patterns are similar to the other non-Newtonian cases.

4.3.2. Vorticity field. (i) $Str = 0.05$: An important aspect for studying the vortex-formation mechanism is the vorticity field. The vorticity is expressed as $\zeta = \partial v/\partial x - \partial u/\partial y$ and its distribution for selected time instants is shown in Figures 3(i), 6(i), 9(i) and 12(i) for the Newtonian, Casson, power-law and Quemada models, respectively. The maximum and minimum vorticity values are also given and between these values are 25 contour increments for all time steps in all cases. Starting from the acceleration phase, increased vorticity is generated at the throat of the constriction and is positive and negative on the lower and upper wall, respectively. This high vorticity is convected downstream by the core flow forming a tongue, which rolls up and forms eddy $A1$ ($t' = 0.7$). The roll up of the vorticity tongue from the

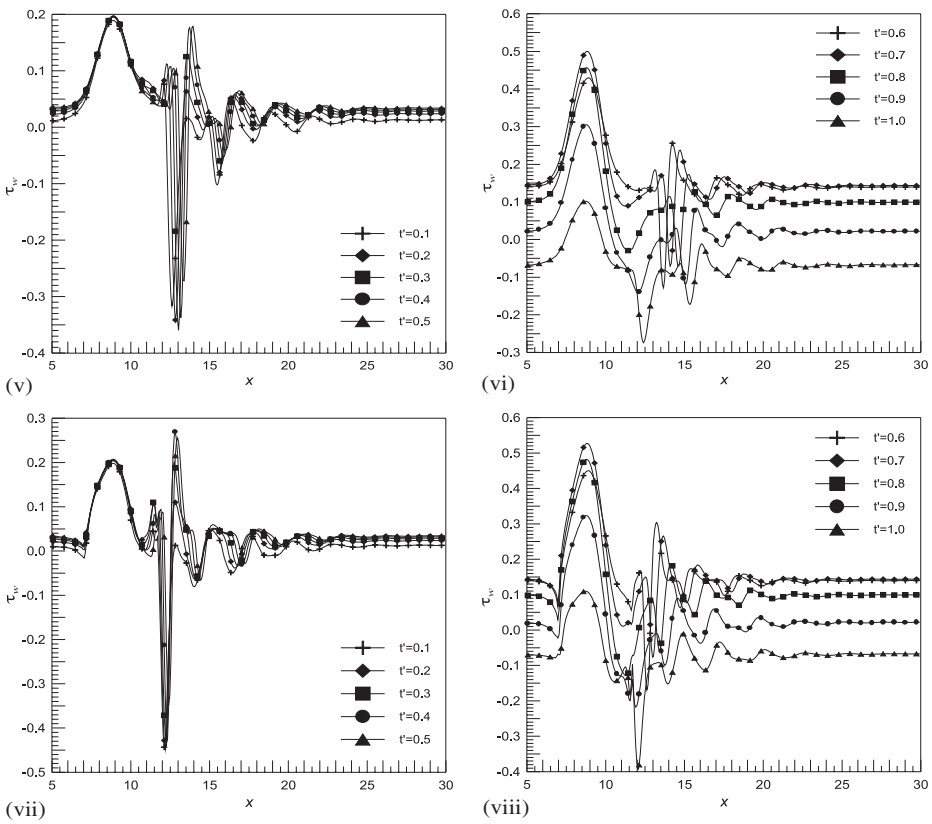

Figure 10. *Continued.*

lower wall creates eddy $B1$. In the deceleration phase the eddy-doubling phenomenon occurs as previously mentioned. This is because vorticity of opposite sign is generated beneath the primary eddy $B1$ owing to the non-slip condition on the wall. This is convected upstream, then towards the centre of the channel and rolls up clockwise forming the counter-rotating secondary eddy. At $t' = 0.9$ the vorticity cancellation induced by the convection of counter vorticity from beneath the primary eddy $B1$ towards the centre of the channel causes the primary eddy to break up into two co-rotating eddies. Furthermore, the vorticity in $A2$ and $B2$ is so intense that the counter vorticity generated between each of the vortices and the wall is sufficient to induce eddy doubling. At the end of the deceleration phase ($t' = 1.0$), eddy break-up through the mechanism of vorticity cancellation, as described above, occurs also at $A2$ and $B2$. It is worthwhile mentioning that for $t' = 1.0$, the maximum and minimum vorticity values are no longer met at the throat of the constriction but beneath and above the primary eddies $B1$ and $A1$, respectively. At the beginning of the steady phase ($t' = 0.1$) the generation of vorticity at the throat is much lower. Therefore, diffusion prevails and since convection is not so strong as to feed the distal eddies with sufficient vorticity, these are starting to dissipate. This is more obvious later ($t' = 0.3$) where the vorticity generation at the throat is on the same levels, whereas, owing to diffusion, the wavy vorticity contours in the core flow

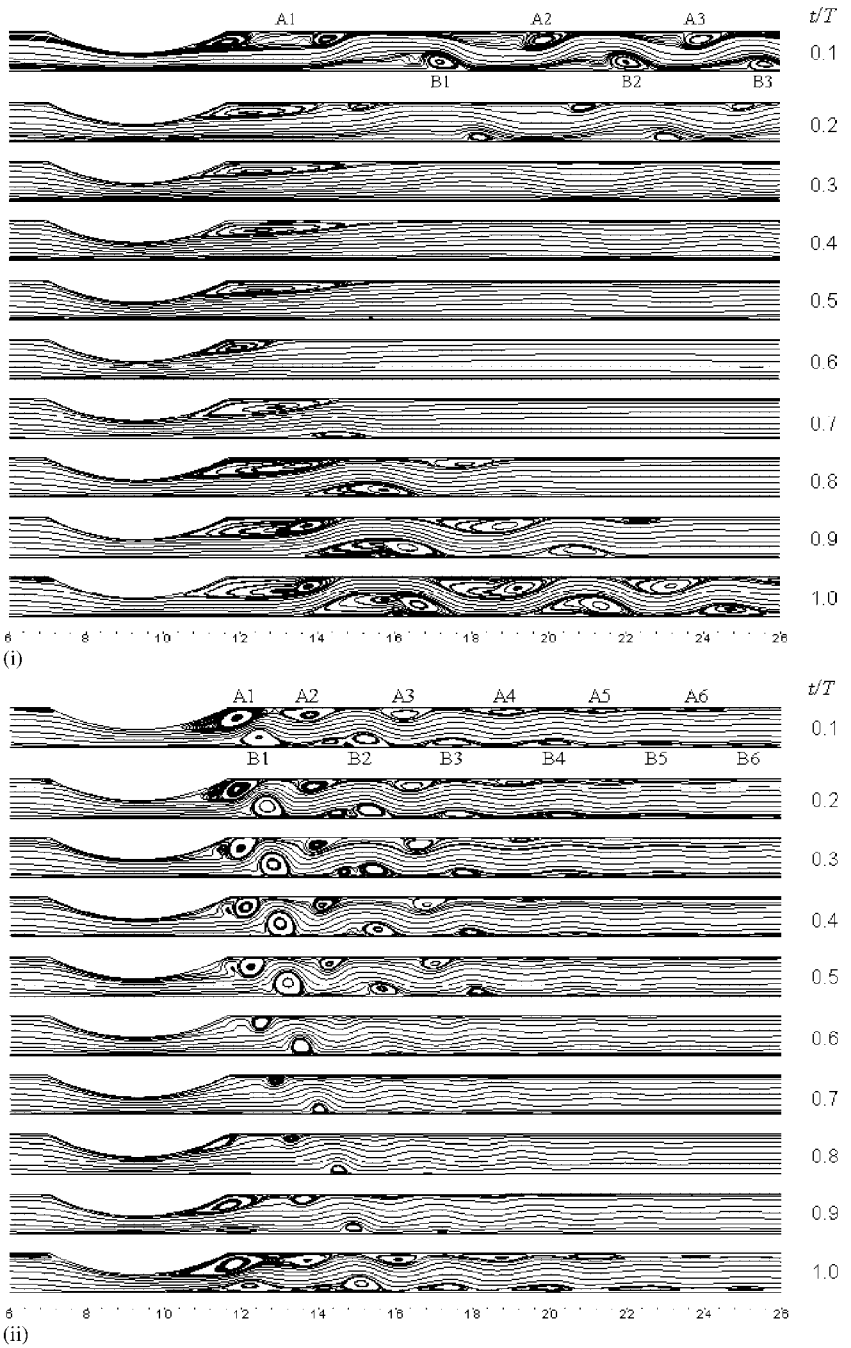

Figure 11. Instantaneous streamlines for a Quemada fluid at $Re_{QU} = 931$, $\gamma_c^* = 0.364$, at selected time instants. (i) $Str = 0.05$. (ii) $Str = 0.368$.

are starting to straighten out. At $t' = 0.5$ the vorticity patterns are very close to stabilization and the two vorticity tongues emerging from the upper and lower walls feed eddies $A1$ and $B1$, respectively. Throughout the steady phase the maximum and minimum values of vorticity are met at the throat and remain practically unchanged during the simulation.

For the Casson model (Figure 6(i)) at the beginning of the acceleration phase the vorticity generated at the throat is on the same level as for the Newtonian flow. The diffusion rate though, is more dominant than in the Newtonian case and this can be seen by comparing the lengths of the vorticity tongues emerging from the throat. These extend to a greater length in the Newtonian case. At the end of the deceleration phase ($t' = 1.0$) the vorticity beneath eddy $B1$ and above $A1$ is more intense than at the throat. The diffusion rates are again strong and this can be seen from the fact that the vorticity beneath $B1$ cannot be convected far towards the centre of the channel so that roll-up can be possible, which would lead to eddy doubling. Vorticity cancellation is evident though, and leads to the break-up of eddies $A1$ and $B1$. This is the only time instant in which the values of maximum and minimum vorticity differ markedly from the corresponding Newtonian values. This is again due to increased diffusion rates. At the beginning of the steady phase ($t' = 0.1$) the vorticity contours are not so 'kinked' as in the Newtonian case, which accounts for the decreased convection rate. The rest of the steady phase is similar to the corresponding Newtonian, but the vorticity contours straighten out more quickly.

For the power-law model (Figure 9(i)), at the beginning of the acceleration phase the vorticity generated at the throat is again on the same level as for the Newtonian flow. In this case the vorticity tongues emerging from the throat extend to an even shorter length than in the Casson and Newtonian cases. The effect of this high diffusion rate is that it is even harder for the vorticity tongues to roll up and create eddies and this can be seen from the fact that no eddy doubling occurs. In fact, for $t' = 1.0$, the high counter vorticity induced from underneath eddy $B1$ is so quickly diffused that no breaking up of eddy $B1$ occurs. During the steady phase the high diffusion rates of vorticity are evident from the less 'kinked' contours. Indeed the contours straighten out more quickly than for the Casson case.

For the Quemada model (Figure 12(i)) the vorticity dissipation rates seem to be between those of the Casson and the Newtonian models. At the beginning of the acceleration phase the length up to which the vorticity tongues extend is between the Newtonian and the Casson cases. The minimum and maximum values of vorticity throughout the cycle are very close to the Casson case. The vorticity contours at the end of the deceleration phase ($t' = 1.0$) are more 'kinked' than in the Casson case, which implies that the dissipation rates are lower. This can also be seen by examining the vorticity contours for the steady phase. These are initially very complex and they do not straighten out so quickly as for the rest of the non-Newtonian models. In fact, they still have to stabilise by the end of the steady phase ($t' = 0.5$).

It is worthwhile mentioning that the minimum and maximum levels of vorticity for the $Str = 0.05$ case, are similar for all the models throughout the cycle except at the end of the deceleration phase. This is due to the fact that at this instant the area where the peak values of vorticity are found is not the same for all models. This can be above and beneath $A1$ and $B1$, respectively, or at the throat of the constriction. In the first case, the dissipation rate is low and therefore high vorticity generated previously still exists. In the second case, the dissipation rate is high and therefore high vorticity from previous instants has already dissipated and the peak values are found at the throat, which is the source of vorticity generation.

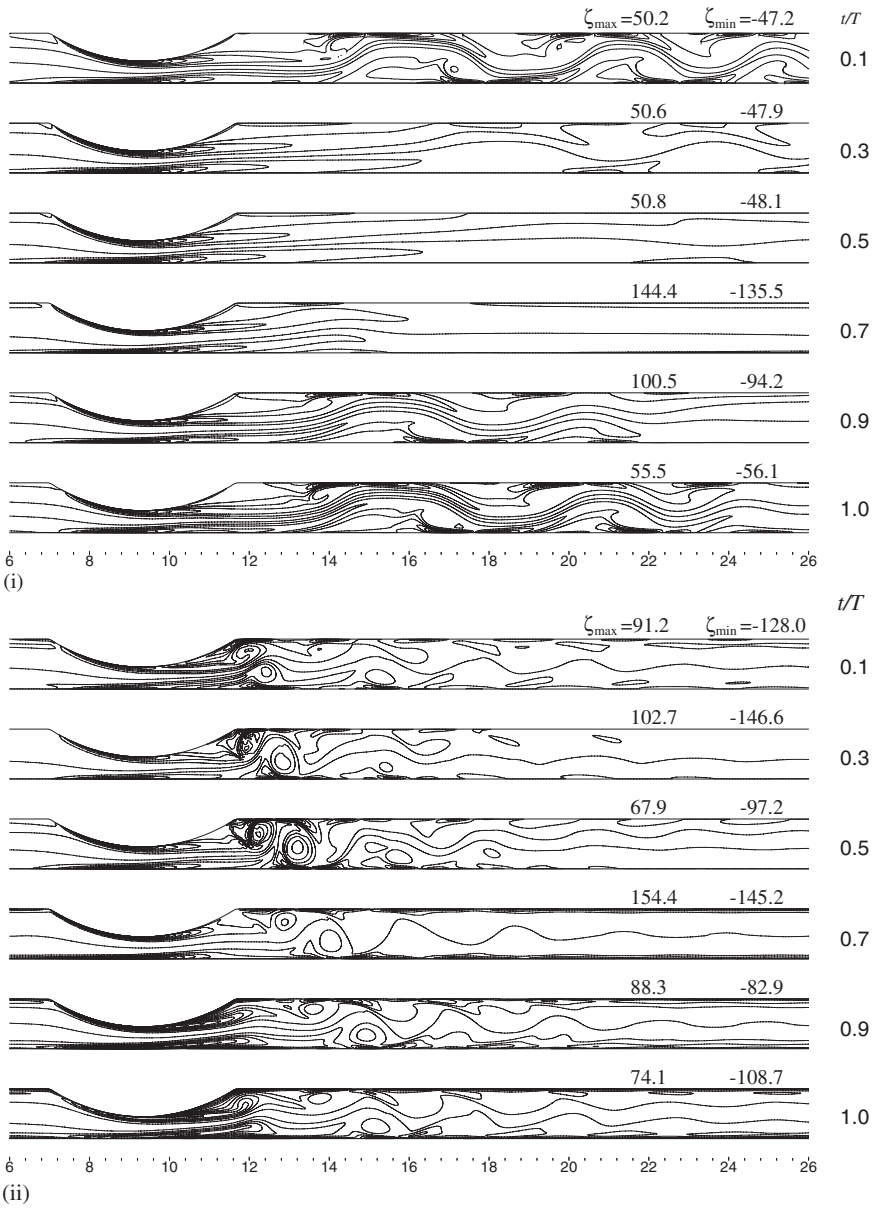

Figure 12. Instantaneous vorticity distribution for a Quemada fluid at $Re_{QU} = 931$, $\gamma_c^* = 0.364$, at selected time instants. (i) $Str = 0.05$. (ii) $Str = 0.368$.

(ii) $Str = 0.368$: The vorticity field for the $Str = 0.368$ case and for selected time instants is shown in Figures 3(ii), 6(ii), 9(ii) and 12(ii) for the Newtonian, Casson, power-law and Quemada models, respectively. Between the maximum and minimum values given for each time instant, there are 30 isocontour increments for all time steps in all cases. The main flow

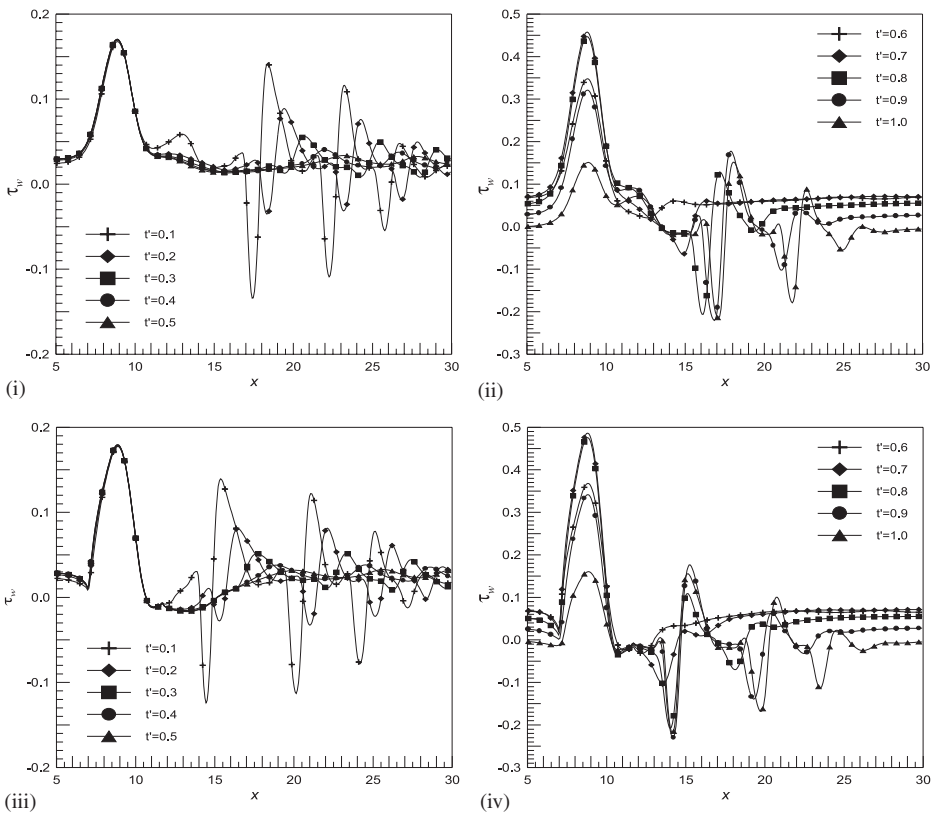

Figure 13. Dimensionless shear stress distribution for a Quemada fluid at $Re_{QU} = 931$, $\gamma_c^* = 0.364$, at selected time instants. (i) Lower wall, $t' = 0.1$–0.5, $Str = 0.05$. (ii) Lower wall, $t' = 0.6$–1.0, $Str = 0.05$. (iii) Upper wall, $t' = 0.1$–0.5, $Str = 0.05$. (iv) Upper wall, $t' = 0.6$–1.0, $Str = 0.05$. (v) Lower wall, $t' = 0.1$–0.5, $Str = 0.368$. (vi) Lower wall, $t' = 0.6$–1.0, $Str = 0.368$. (vii) Upper wall, $t' = 0.1$–0.5, $Str = 0.368$. (viii) Upper wall, $t' = 0.6$–1.0, $Str = 0.368$.

phenomena will be described for the case of the Newtonian model (Figure 3(ii)). Starting from the acceleration phase, the vorticity generation is stronger than for $Str = 0.05$. The highest vorticity level occurs on the upper wall of the throat of the constriction and the lowest level on the lowest wall. These intense vorticity tongues extend to a distance downstream of the constriction and their subsequent roll-up forms the eddies shown in Figure 2(ii). The vorticity generation is more intense than in the case of $Str = 0.05$ and that is due to the higher acceleration rate. For $t' = 0.7$ the maximum and minimum vorticity levels are again higher as regards absolute values than for $Str = 0.05$ and are found in the same positions at the throat of the constriction. At the beginning of the deceleration phase the vorticity levels generated at the throat start to drop owing to the decreasing of the inflow rate. This drop continues until the end of the deceleration phase ($t' = 1.0$) and the maximum and minimum levels of vorticity are no longer found at the throat of the constriction but beneath $B1$ and above $A1$, respectively. At the beginning of the steady phase ($t' = 0.1$) the vorticity generation at the throat drops

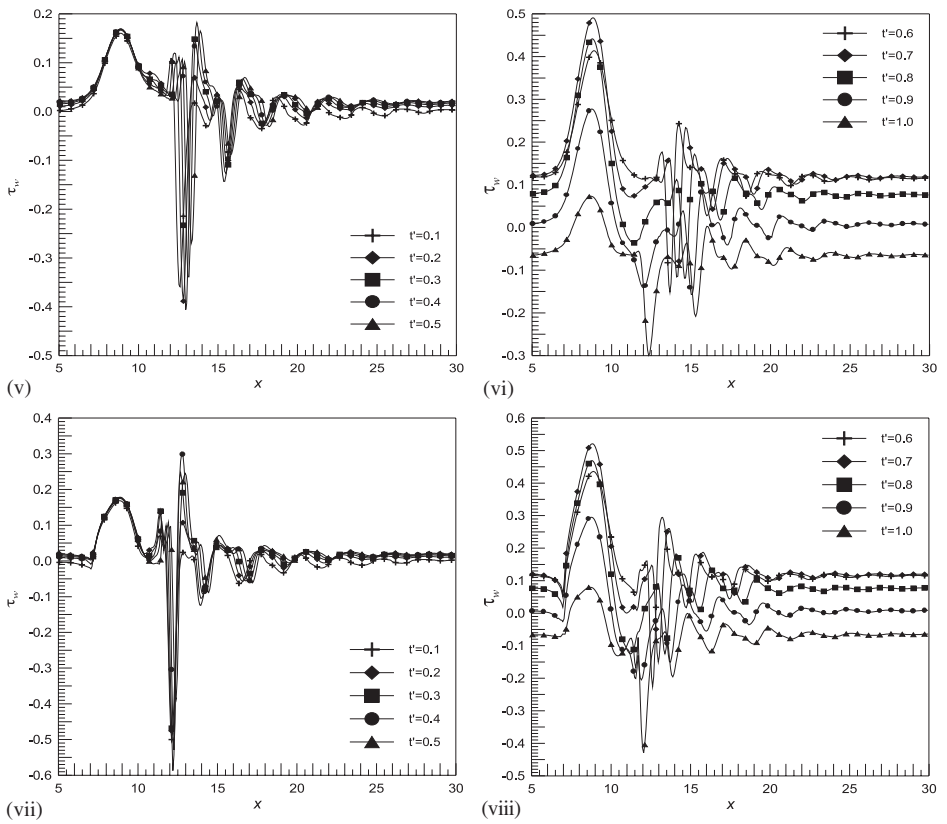

Figure 13. *Continued.*

even more while the levels of vorticity above and beneath $A1$ and $B1$, respectively, continue to rise until $t' = 0.3$. This is due to the accumulation of transient effects from the second half of the previous cycle which are more intense than for $Str = 0.05$. The mechanisms of vorticity generation and diffusion described previously for $Str = 0.05$ cause eddy doubling and eddy break-up for eddies $A1$ and $B2$. At $t' = 0.4$ and while vorticity generation at the throat remains unaltered, the vorticity levels above $A1$ and beneath $B1$ begin to drop. This is due to the fact that diffusion mechanisms dominate at the later stages of the steady phase.

In the case of the Casson model (Figure 6(ii)), at the beginning of the acceleration phase the vorticity generation at the throat is slightly lower than for the Newtonian case and it remains so until the end of the deceleration phase ($t' = 1.0$). During the steady phase, the vorticity levels beneath $B1$ and above $A1$ prevail over the vorticity levels at the throat but are much weaker compared to the Newtonian case. Their strength though, is sufficient to induce eddy-doubling and eddy-breaking phenomena.

In the case of the power-law model (Figure 9(ii)), at the beginning of the acceleration phase the vorticity generation at the throat is the highest among all the models. A rapid drop follows, which by the end of the deceleration phase ($t' = 1.0$) brings the peak values of vorticity to their lowest level among all models. During the steady phase ($t' = 0.1$–0.5), the

vorticity levels are still the weakest compared to the rest of the models and this accounts for the high diffusion mechanisms that occur for the power-law model. Eddy doubling occurs for $A1$ but not for $B2$, in the area of which the convection and diffusion of the vorticity from beneath induces eddy breaking only.

In the case of the Quemada model (Figure 12(ii)), at the beginning of the acceleration phase the maximum and minimum vorticity levels are slightly weaker than for the Newtonian case and are very close to the Casson model. The same applies to the deceleration and steady phases where the vorticity peak levels are between the Casson and Newtonian cases.

4.3.3. Wall shear stress. (i) $Str = 0.05$: From the physiological point of view, the wall shear stress is a very important factor. The dimensionless wall shear stress (DWSS) distributions on the lower and upper wall for the $Str = 0.05$ case are shown in Figures 4(i)–4(iv) for the Newtonian model, 7(i)–7(iv) for the Casson model, 10(i)–10(iv) for the power-law model and 13(i)–13(iv) for the Quemada model.

The distribution on the lower and upper walls, for all models, shows certain similarities. First, there are large variations in the DWSS distribution in the vicinity of the stenosis, caused by the unsteadiness of the inflow rate in conjunction with the existence of a stenotic segment. During the steady phase there is a maximum of the DWSS at the throat of the constriction, the value of which remains unchanged throughout the whole phase. At the beginning of the steady phase ($t' = 0.1$) large variations in the DWSS appear downstream of the constriction owing to the existing eddies. Local minimum peaks correspond to the interaction between an eddy and the wall and maximum peaks correspond to the diversion of the core flow onto the wall owing to the existence of an eddy on the opposite wall. These peak values move progressively downstream and become lower in agreement with the eddy propagation and diffusion. By the end of the steady phase ($t' = 0.5$) the peaks downstream diminish and only the maximum peak at the throat of the constriction is evident. At the beginning of the acceleration phase ($t' = 0.6$) the DWSS values along the wall are higher. This is obvious in the case of the peak value at the throat of the constriction. Later at $t' = 0.7$ the peak value at the constriction reaches its highest value and at the beginning of the deceleration phase ($t' = 0.8$) the peaks of the DWSS distribution downstream of the constriction are starting to develop. These become progressively more intense ($t' = 0.9$) and gain their highest levels (as regards absolute values) at the end of the deceleration phase ($t' = 1.0$) whereas the peak at the throat of the constriction drops to its lowest level throughout the cycle.

Although the distribution is similar for all the models, the peak values of the DWSS for every model throughout the cycle are markedly different. Table I gives the maximum and minimum values of the DWSS under stenotic ($(\mathrm{DWSS}_{\max})_{\mathrm{st}}$ and $(\mathrm{DWSS}_{\min})_{\mathrm{st}}$) and under normal ($(\mathrm{DWSS}_{\max})_n$ and $(\mathrm{DWSS}_{\min})_n$) conditions on the upper and lower walls, for all models. Normal conditions imply a channel with no stenosis but the same inflow boundary conditions. The distance and time instants at which the values are found are also given.

For normal conditions, it can be seen that the values of $\mathrm{DWSS}_{\max}$ and $\mathrm{DWSS}_{\min}$ throughout the cycle are similar for all models and the time instant at which they occur is identical. The effects under stenotic conditions are markedly different. $(\mathrm{DWSS}_{\max})_{\mathrm{st}}$ on the lower wall is lower for the Newtonian case and almost the same for the non-Newtonian models. The distance and time instant at which it occurs is the same for all models. The absolute value of $(\mathrm{DWSS}_{\min})_{\mathrm{st}}$ on the lower wall takes its largest value for the Newtonian model and its smallest value for the power-law model. Moreover, the distance at which it occurs is shorter for the

Table I. Peak values of DWSS on the lower (Lo) and upper (Up) walls under stenotic and normal conditions for $Str = 0.05$.

		Newtonian			Casson			Power law			Quemada		
		Value	x'	t'	Value	x'	t'	Value	x'	t'	Value	x'	t'
Lo	$(DWSS_{max})_{st}$	0.40	8.8	0.7	0.47	8.8	0.7	0.47	8.8	0.7	0.46	8.8	0.7
	$(DWSS_{min})_{st}$	−0.24	17.0	0.9	−0.21	16.7	0.9	−0.17	16.6	0.9	−0.22	16.7	0.9
Up	$(DWSS_{max})_{st}$	0.43	8.8	0.7	0.50	8.8	0.7	0.50	8.8	0.7	0.49	8.8	0.7
	$(DWSS_{min})_{st}$	−0.23	14.4	0.9	−0.22	14.2	0.9	−0.20	14.0	0.9	−0.23	14.2	0.9
	$(DWSS_{max})_{n}$	0.05	—	0.7	0.08	—	0.7	0.09	—	0.7	0.07	—	0.7
	$(DWSS_{min})_{n}$	−0.01	—	1.0	0	—	1.0	0.01	—	1.0	0	—	1.0

non-Newtonian models. Similarly, on the upper wall $(DWSS_{max})_{st}$ takes its smallest value for the Newtonian models but the values for all models are higher than the corresponding ones on the lower wall, although they occur at the same distance and time instant. The absolute value of $(DWSS_{min})_{st}$ on the upper wall is very close for the Newtonian, Casson and Quemada models and is slightly lower for the power-law model. The distance at which it occurs is identical for the Casson and Quemada models and the time at which it occurs is identical for all models.

Another important aspect that should be taken into account, owing to its haemodynamic effects in realistic conditions, is the amplitude of the oscillating DWSS at a certain point on the wall. Table II gives the values of the maximum amplitudes (A_{max}) of the DWSS on the upper and lower walls for all models throughout the cycle and the distances at which these occur.

On the lower wall, the amplitude is greatest for the Newtonian model followed, in order of decreasing magnitude, by the Quemada, then the Casson and finally the power-law model. It can be seen that the distance at which A_{max} occurs is at a point downstream of the constriction and is similar for all models except the power-law model in the case of which A_{max} occurs at the throat of the constriction. This phenomenon of A_{max} being greater upstream is related to the eddy-propagation phenomenon. For example, at a certain point there is a positive peak of DWSS due to diversion of the core flow towards it because of the presence of an eddy on the opposite wall. Later, owing to eddy propagation, a negative peak of DWSS will occur at this point owing to a forthcoming eddy that now occupies the point. This can also be seen in Figure 4(ii) for the point $x' = 17.1$ between $t' = 0.8$ and 1.0. This phenomenon, though evident in the cases of the Newtonian, Casson and Quemada models, does not occur for the power-law model because of the rapid dissipation of eddies.

On the upper wall A_{max} occurs at the throat of the constriction and its values are similar for all models. This value of A_{max} for the Newtonian case is much lower than for the lower wall. This is not true for the non-Newtonian models in the case of which the values of A_{max} for the upper and lower walls are similar.

(ii) $Str = 0.368$: The DWSS distribution on the lower and upper wall for the $Str = 0.368$ case is shown in Figures 4(v)–4(viii) for the Newtonian model, 7(v)–7(viii) for the Casson model, 10(v)–10(viii) for the power-law model and 13(v)–13(viii) for the Quemada model.

Table II. Amplitude of the DWSS on the lower and upper walls under stenotic conditions for $Str = 0.05$.

		Newtonian		Casson		Power law		Quemada	
		Value	x'	Value	x'	Value	x'	Value	x'
A_{max}	Lower W	0.39	17.3	0.31	17.1	0.29	8.8	0.34	17.1
	Upper W	0.30	8.7	0.33	8.7	0.31	8.7	0.33	8.7

The general phenomena in the DWSS distribution occurring for all models are described below. During the steady phase, large variations in the DWSS occur for both the lower and the upper walls as a result of the unsteadiness of the inflow rate and the presence of the constriction. First, a peak in the distribution can be seen at the throat of the constriction that remains unaltered throughout the steady phase. Further downstream the fluctuations are time dependent and the peak values are due to the presence of eddies. These fluctuations are much more intense than for $Str = 0.05$ and this is due to the stronger eddies formed as a result of the higher deceleration rates. The most prominent peaks in the distribution are the minimum ones occurring just after the stenosis, corresponding to eddies $A1$ and $B1$ on the upper and lower walls, respectively. Every peak value changes as a function of time according to the eddy-strength change. The peaks of DWSS, as previously mentioned for $Str = 0.05$, correspond to the core flow being diverted towards the wall owing to the existence of an eddy at the opposite wall. During the steady phase, the smallest value of the DWSS occurs at $t' = 0.3$ for both the upper and the lower wall. At the beginning of the acceleration phase ($t' = 0.6$) the peak value at the throat rises while the peak values downstream of the constriction become weaker. The peak at the throat at $t' = 0.7$ reaches its maximum value throughout the cycle and then drops progressively in the deceleration phase. It reaches its minimum value throughout the cycle at the end of the deceleration phase ($t' = 1.0$).

Despite the similarities in the distribution of the DWSS between the models, the differences between the peaks that each model exhibits are most important. These peak values are given in Table III for DWSS under stenotic and normal conditions (the nomenclature used in the table is the same as for $Str = 0.05$) along with the time instant and distance at which these are found.

Under normal conditions the $DWSS_{min}$ is practically the same for all models and $DWSS_{max}$ is slightly higher in the cases of the non-Newtonian models. In addition, the time instants, at which each of the $DWSS_{min}$ and $DWSS_{max}$ are found, are the same for all models. At stenotic conditions, marked differences are evident between the peak values of DWSS that each model exhibits. On the lower wall $DWSS_{max}$ is found at the throat of the constriction at $t' = 0.7$, for all models. The values for the non-Newtonian models are very close, but far from the Newtonian case for which $DWSS_{max}$ is lower. $DWSS_{min}$ is found at the same distance and time instant for all models and the values are very close for all models with the exception of the power-law case for which the value is slightly higher. On the upper wall the results for $DWSS_{min}$ are similar to the results for the lower wall. The values of $DWSS_{min}$ are again very close for the non-Newtonian models and far from the value for the Newtonian case, which is lower. The peak values for all models occur at the same distance and time instant. In the case of $DWSS_{max}$ there are substantial differences between the models. The Newtonian model has the lowest value, followed by the Quemada, then the Casson and finally the power-law

Table III. Peak values of DWSS on the lower (Lo) and Upper (Up) walls under stenotic and normal conditions for $Str = 0.368$.

		Newtonian			Casson			Power law			Quemada		
		Value	x'	t'	Value	x'	t'	Value	x'	t'	Value	x'	t'
Lo	$(DWSS_{max})_{st}$	0.43	8.8	0.7	0.51	8.8	0.7	0.50	8.8	0.7	0.49	8.8	0.7
	$(DWSS_{min})_{st}$	−0.40	13.0	0.3	−0.39	13.0	0.3	−0.36	13.0	0.3	−0.41	13.0	0.3
Up	$(DWSS_{max})_{st}$	0.46	8.8	0.7	0.54	8.8	0.7	0.53	8.8	0.7	0.52	8.8	0.7
	$(DWSS_{min})_{st}$	−0.65	12.2	0.3	−0.53	12.2	0.3	−0.45	12.2	0.2	−0.59	12.2	0.3
	$(DWSS_{max})_{n}$	0.10	—	0.7	0.13	—	0.7	0.14	—	0.7	0.12	—	0.7
	$(DWSS_{min})_{n}$	−0.06	—	1.0	−0.07	—	1.0	−0.07	—	1.0	−0.07	—	1.0

Table IV. Amplitude of the DWSS on the lower and upper walls under stenotic conditions for $Str = 0.368$.

		Newtonian		Casson		Power law		Quemada	
		Value	x'	Value	x'	Value	x'	Value	x'
A_{max}	Lower W	0.49	13.0	0.49	13.0	0.44	12.8	0.50	12.8
	Upper W	0.57	12.0	0.59	12.0	0.53	12.1	0.60	12.1

model, which exhibits the lowest in absolute peak value. The distance and time instant at which the peak values occur are again the same for all models.

Table IV gives the values of the maximum amplitude (A_{max}) of the oscillating DWSS for all models. It can be seen that the values of A_{max} at both the upper and lower wall are much higher than the corresponding ones for $Str = 0.05$. At the lower wall the values are very close for all models except the power-law model, which exhibits smaller values. The distance, at which A_{max} occurs, is practically the same for all models. The same applies to the upper wall but the amplitudes occurring there are higher than those on the lower wall. The Newtonian, Casson and Quemada models seem to have similar behaviour in terms of A_{max}, while A_{max} for the power-law model is always lower.

5. CONCLUSIONS

In this paper, the flow in a stenotic channel was studied using the Newtonian and three non-Newtonian models, namely the Casson, power-law and Quemada models. Three different flow cases were considered: a steady case with $Re = 360$ and two unsteady cases with the same Re number but different Strouhal numbers, namely $Str = 0.05$ and 0.368. The calculation of the corresponding non-Newtonian parameters was carried out assuming the same inflow rate. The results show that for $Str = 0.368$ the flow does not stabilize at the end of the steady phase. Furthermore, the number of eddies at the steady state is significantly lower for $Str = 0.05$ and decreases progressively throughout the phase. This decrease is more evident in the case of the non-Newtonian models. Eddy breaking and eddy doubling are more intense for $Str = 0.05$. For the non-Newtonian models these phenomena develop to a lesser extent.

For the unsteady flow, the acceleration phase contributes to the decrease of the number of eddies for both unsteady flow cases and for all models. The deceleration phase though, is different between the two unsteady cases. For $Str = 0.368$ more crests and troughs occur in the flow owing to the more rapid deceleration and to the fact that the width of the core flow is greater. The opposite happens for $Str = 0.05$ where the crests and troughs are fewer in number. For the Quemada and Casson models the phenomena of eddy breaking and eddy doubling appear to a similar extend and are weaker in the power-law model.

As far as the vorticity generation is concerned, for $Str = 0.05$, at the beginning of the steady phase the highest absolute vorticity values are found at the throat of the constriction, while for $Str = 0.368$ these are met above and beneath eddies $A1$ and $B1$, respectively. The power-law model generates higher vorticity at the throat of the constriction during the acceleration phase whereas these high levels of vorticity drop rapidly and fall below the corresponding levels for the rest of the models during the steady phase. The vorticity levels for the Casson and Quemada models are similar and lower than the Newtonian model throughout the cycle.

Regarding the DWSS distribution, this is uniform and similar for all models under non-stenotic conditions. At stenotic conditions the most intense fluctuations occur on the upper wall in both unsteady cases. Throughout the cycle the maximum value of DWSS occurs at the throat and the minimum value in the lee of the constriction. Although with respect to the maximum values of DWSS for the unsteady cases the models do not differ, they exhibit differences regarding the minimum values, especially for $Str = 0.368$.

The locations, at which the peak values of DWSS and the maximum amplitudes $A_{\max}$ occur, are at the throat and in the lee of the constriction. In physiogical flows this may lead to the narrowing and elongation of the stenosis. According to Fry [22], DWSS variations up to the extent reported here can cause irreversible damage to the endothelial lining. This leads to the hypothesis that variations of DWSS at the wall without the stenosis, caused by the stenosis at the opposite wall, can initiate atheroma formation at an area just opposite the area where atheroma already exists, leading to precipitation of the occlusion process in the diseased vessel.

REFERENCES

1. Charm S, Kurland G. Viscometry of human blood for shear rates of 0-100,000 $\sec^{-1}$. *Nature* 1965; **206**: 617–618.
2. Nerem RM, Mosberg AT, Schwerin WD. Transendothelial transport of ^{131}I-albumin. *Biorheology* 1976; **13**: 71–77.
3. Fry DL. Acute vascular endothelial damages associated with increased blood velocity gradients. *Circulation Research* 1968; **22**:165–197.
4. Rosenfeld M. Validation of numerical simulation of incompressible pulsatile flow in a constricted channel. *Computers and Fluids* 1993; **22**:139–156.
5. Rosenfeld M. Numerical study of pulsating flow behind a constriction. *Journal of Fluid Mechanics* 1995; **301**:203–223.
6. Rosenfeld M, Einav S. The effect of constriction size on the pulsatile flow in a channel. *Transactions of the ASME Journal of Fluids Engineering* 1995; **117**:571–576.
7. Tutty OR. Pulsatile flow in a constricted channel. *Transactions of the ASME Journal of Biomechanical Engineering* 1992; **114**:50–54.
8. Mallinger F, Drikakis D. Instability in three-dimensional, unsteady stenotic flows. *International Journal for Heat and Fluid Flow* 2002; **23**:657–663.
9. Tu C, Deville M. Pulsatile flow of non-Newtonian fluids through arterial stenoses. *Journal of Biomechanics* 1996; **29**:899–908.
10. Yamaguchi R. Distribution of mass transfer rate and wall shear stress behind simple rectangular stenosis in pulsating flow. *Transactions of the ASME Journal of Biomechanical Engineering* 1989; **111**:47–54.
11. Drikakis D. Bifurcation phenomena in incompressible sudden expansion flows. *Physics of Fluids* 1997; **9**: 76–87.

12. Ang KC, Mazumdar JN. Mathematical modelling of three-dimensional flow through an asymmetric arterial stenosis. *Mathematical Computer Modelling* 1997; **25**:19–29.
13. Buchanan Jr JR, Kleinstreuer C, Comer JK. Rheological effects on pulsatile hemodynamics in a stenosed tube. *Computers and Fluids* 2000; **29**:695–724.
14. Srivastava VP, Saxena M. Two-layered model of casson fluid flow through stenotic vessels: applications to the cardiovascular system. *Journal of Biomechanics* 1994; **27**:921–928.
15. Sherwin SJ, Peiró J, Shah O, Karamanos G-S, Doorly DJ. Computational haemodynamics: geometry and non-Newtonian modelling using spectral/hp element methods. *Comparative Visual Science* 2000; **3**:77–83.
16. Casson NA. A flow equation for pigment-oil suspensions of the printing ink type. *Rheology of Disperse Systems*. Mills CC (ed.). Pergamon: Oxford, 1959; 84–102.
17. Walburn FJ, Schneck DJ. A constitutive equation for whole human blood. *Biorheology* 1976; **13**:201–210.
18. Quemada D. Rheology of concentrated disperse systems III. General features of the proposed non-newtonian model. Comparison with experimental data. *Rheologica Acta* 1977; **17**:643–653.
19. Charm SE, McComis W, Kurland G. Rheology and structure of blood suspension. *Journal of Applied Physiology* 1964; **19**:127–133.
20. Papanastasiou TC. Flow of materials with yield. *Journal of Rheology* 1987; **31**:385–404.
21. Pham TV, Mitsoulis E. Entry and exit flows of Casson fluids. *The Canadian Journal of Chemical Engineering* 1994; **17**:1080–1084.
22. Ferziger JH, Peric M. *Computational Methods for Fluid Dynamics*. Springer: Berlin, 1999.
23. Patankar SV, Spalding DB. A calculation procedure for heat, mass and momentum transfer in three dimensional parabolic flows. *International Journal of Heat Mass Transfer* 1972; **15**:1787–1806.
24. Stone HL. Iterative solution of implicit approximations of multidimensional partial differential equations. *SIAM Journal on Numerical Analysis* 1968; **5**:530–558.
25. Spiller P, Schmiel FK, Pöntz B, Block M, Fermor U, Hackbarth W, Jehle J, Körfer R, Pannek H. Measurement of systolic and diastolic flowrates in coronary artery system by X-ray densitometry. *Circulation* 1983; **68**: 337–347.
26. Park DK. A biofluid mechanics study of arterial stenoses. *M.Sc. Thesis*, Lehigh University, Bethlehem, PA, 1989.
27. Batchelor GK. *An Introduction to Fluid Mechanics*. Cambridge University Press: Cambridge, MA, 1967.
28. Cornhill JF, Roach MR. A quantitative study of the localisation of atherosclerotic lesions in the rabbit aorta. *Atherosclerosis* 1976; **23**:489–501.
29. Neofitou P, Drikakis D, Leschziner MA. Study of Newtonian and non-Newtonian flow in a channel with a moving indentation. In *Proceedings of the IMA conference on Cardiovascular Flow Modelling and Measurement with Application to Clinical Medicine*, Sajjadi SG *et al.* (eds). Clarendon: Oxford, 1999; 39–47.

